Untangling cosmic collisions: a study of particle acceleration and magnetic fields in merging galaxy clusters

Osinga, E.

6

Probing cluster magnetism with embedded and background radio sources in Planck clusters

Magnetic fields remain an enigmatic part of the non-thermal content of galaxy clusters. Faraday rotation and depolarisation of extragalactic radio sources are useful probes, but the limited availability of polarised radio sources necessitates the stacking of clusters to study average magnetic field profiles and correlation scales. In this study, we combine the information from depolarisation with the observed rotation measure (RM) and present an investigation into the average magnetic field properties of the most massive Planck clusters at low redshift ($z < 0.35$), using both background sources and sources embedded in clusters. As expected for randomly oriented magnetic fields, we find an average RM consistent with zero as a function of projected radius, but observe a significant increase in the RM scatter, $\sigma_{\rm RM}$, closer to the cluster centres. Averaging all 124 clusters, we find a scatter within R_{500} of $\sigma_{\rm RM} = 241 \pm 44$ rad m^{-2}. In the simple assumption of a uniform magnetic field with a single fluctuation scale Λ_c, this translates to an average magnetic field strength of $3\,(\Lambda_c/10{\rm kpc})^{-0.5}\,\mu G$. Because the highest RM sources near the centre of clusters are depolarised, the radial profile of $\sigma_{\rm RM}$ puts a lower limit on the scaling between the magnetic field and thermal gas density of $\eta > 0.15$. Combining depolarisation and RM in a full forward model, we find that the observations best agree with a magnetic field that fluctuates on a maximum scale $\Lambda_{\rm max} > 300$ kpc and follows a power spectrum with exponent $n = 3$ to $n = 4$, consistent with Kolmogorov turbulence injected on large scales. The best-fit average magnetic field profile is equal to $B_0 = 5\,\mu G$ in the centre, declining with radius as $B(r) \propto n_e(r)^{0.5}$.

Based on Osinga et al. (2023b): *E. Osinga, R. J. van Weeren, L. Rudnick, F. Andrade-Santos, A. Bonafede, T. Clarke, K. Duncan, S. Giacintucci, Tony Mroczkowski, H. J. A. Röttgering, A&A to be subm.*

6.1 Introduction

Galaxy clusters, the largest gravitationally bound structures in the Universe, harbour a rich variety of physical phenomena. Radio observations have revealed that clusters often show diffuse synchrotron emission that can span Mpc-sized regions, such as 'radio halos' (e.g. Bonafede et al., 2022) or 'mega-halos' (Cuciti et al., 2022), implying that clusters are filled with ultra-relativistic electrons and magnetic fields. The influence of the magnetic fields extends to particle acceleration models, radio synchrotron age estimates, the dynamics of the intracluster medium (ICM) and the transport of cosmic rays. Understanding the properties and origins of magnetic fields in clusters thus has broad importance (see Carilli & Taylor, 2002; Govoni & Feretti, 2004; Donnert et al., 2018, for reviews on magnetic fields in galaxy clusters).

The most promising tool to study magnetic fields is radio polarisation observations of Faraday rotation and depolarisation. A magnetised plasma such as the ICM causes a wavelength-dependent rotation of the polarisation angle. In general, the Faraday depth of a source is defined as (Burn, 1966; Brentjens & de Bruyn, 2005)

$$\phi(\mathbf{r}) = 812 \int n_e \mathbf{B} \cdot d\mathbf{r} \,\mathrm{rad\,m^{-2}}, \tag{6.1}$$

where n_e is the electron density in parts per cm^{-3}, $\mathbf{B}$ is the magnetic field in μGauss and d$\mathbf{r}$ the infinitesimal path length increment along the line of sight in kpc, and we define $\phi(\mathbf{r}) > 0$ for the magnetic field pointing towards the observer. In the simple case of just one radio-emitting source along the line of sight, the Faraday depth is equal to the rotation measure (RM). With a combination of radio and X-ray observations, it is thus possible to study the magnetic field properties of galaxy clusters.

Such studies are best done at low redshifts, due to the rarity of polarised radio sources (e.g. Rudnick & Owen, 2014). The most detailed analyses have been of the Coma Cluster (Bonafede et al., 2010) and Abell 2345 (Stuardi et al., 2021), where seven radio sources were detected per cluster. The Coma Cluster magnetic field was found to agree with a Kolmogorov power spectrum with a central strength of 5 μG and a scaling of magnetic field energy density linearly proportional to the thermal gas density ($B^2 \propto n_e$). The central magnetic field strength in Abell 2345 was found to be similar to the Coma Cluster, but with a magnetic field energy density that scales super-linear instead (i.e. $B^2 \propto n_e^2$). Several other low-redshift clusters have been analysed in polarisation (Murgia et al., 2004; Govoni et al., 2006; Guidetti et al., 2008; Govoni et al., 2010; Vacca et al., 2012; Govoni et al., 2017), with typically less than five polarised radio galaxies per study, resulting in large uncertainties on the magnetic field estimates (see e.g. Johnson et al., 2020, for a detailed discussion).

Because cluster magnetic fields are thought to be generally turbulent and disordered, the observed Faraday rotation is the result of a random walk process and thus a random variable. Accurate magnetic field estimates, therefore, require a statistical analysis probing many independent sight lines. Another potential problem is that polarised radio galaxies are often embedded in the cluster, and the degree to which the observed RM variations are caused by local interaction of the lobes with the ICM is debated (Laing et al., 2008; Guidetti et al., 2012; Osinga et al., 2022). Such problems can be overcome by stacking clusters to increase the number of polarised radio sources located behind clusters and thus independent sight lines through a cluster (Clarke et al., 2001; Bonafede et al., 2011;

Böhringer et al., 2016; Stasyszyn & de los Rios, 2019; Osinga et al., 2022). Although stacking experiments have limited ability to probe differences between clusters, they are useful for obtaining average cluster magnetic field properties, and are currently the only way to study clusters beyond the few nearest clusters.

We recently published, in Osinga et al. (2022), the largest homogeneous stacking experiment using Karl G. Jansky Very Large Array (VLA) observations of 124 galaxy clusters selected from the Planck 2nd Sunyaev-Zeldovich Source Catalog (PSZ2) (Planck Collaboration et al., 2016a). This study presented the first clear depolarisation trend tracing the radial profile of cluster magnetic fields using over 600 polarised radio sources. While depolarisation traces the smaller scale structure of the magnetic fields (i.e. few kpc), the larger scale structure can be inferred from the Faraday rotation of the radio sources. In this paper, we add the information from the Faraday rotation of the same sample of sources to study the large-scale properties of the magnetic fields in galaxy clusters. By jointly fitting both depolarisation and Faraday rotation, we aim to constrain the average magnetic field strength, scaling with density, and power spectrum. Cosmological calculations are performed assuming a flat ΛCDM model with $H_0 = 70$ kms^{-1}Mpc^{-1}, $\Omega_m = 0.3$ and $\Omega_\Lambda = 0.7$.

6.2 Chandra-Planck ESZ sample

The sample of galaxy clusters is a subset of 124 out of 165 clusters from the *Chandra-Planck Legacy Program for Massive Clusters of Galaxies*[1] (Andrade-Santos et al., 2021) that have VLA observations presented in Osinga et al. (2022). The full details on the data reduction, polarised source identification and association, and determination of the polarisation properties are presented in the aforementioned paper, but we briefly summarise the important points here and highlight some improvements to the catalogue.

Each of the 124 clusters was observed for ∼ 40 min each in the VLA L-band (1–2GHz), resulting in typically 20–30 μJy beam^{-1} noise levels at a resolution of 6–7″ after data reduction. Polarised sources were identified using RM-synthesis (Brentjens & de Bruyn, 2005) and matched to total intensity components and optical counterparts. In total 6,807 and 819 source components were detected in total and polarised intensity respectively. We have fit the following model to the polarised intensity as a function of wavelength λ, which accounts for rotation and depolarisation (see Sokoloff et al., 1998, for details),

$$P(\lambda^2) = p_0 I \exp(-2\sigma_{\rm RM}^2\lambda^4)\exp[2i(\chi_0 + \phi\lambda^2)], \tag{6.2}$$

where p_0 denotes the intrinsic polarisation and $\sigma_{\rm RM}^2$ the variance of the RM distribution which models the depolarisation as a function of wavelength. χ_0 is the intrinsic polarisation angle, and I denotes the total intensity model, which was assumed to be a simple power-law of the form $I(\nu) = I_0\nu^\alpha$.

We have improved the Monte Carlo Markov chain (MCMC) fitter used in Osinga et al. (2022) to now properly take into account the circular nature of χ_0 during the fitting. In Osinga et al. (2022), the prior on χ_0 was uniform $\sim \mathcal{U}(0,\pi)$, which would cause the sampler in some cases to get stuck around the boundary values. We removed this prior on χ_0 and fold the chain back into the range $[0,\pi)$ after the sampling is completed. We also calculate the mean and spread using circular statistics where we take into account the fact that the

[1] http://hea-www.cfa.harvard.edu/CHANDRA_PLANCK_CLUSTERS/

angles are distributed on the half-circle $\in [0, \pi)$. In this way, the mean denotes the angle of the average vector on the unit circle, and the standard deviation is the spread in angles around the average vector. This agrees with the definition of the simple arithmetic mean and standard deviation when the angles are distributed away from the edges of the domain.

This paper is thus accompanied by an updated table of polarised components, shown in Appendix 6.6. We note that this update mainly corrects the quoted mean and uncertainty of the intrinsic polarisation angle χ_0 and most sources have similar best-fit RM and depolarisation parameters. This thus does not significantly impact the results. Finally, we used the same criteria for identifying bad fits as Osinga et al. (2022). All sources with a best-fit χ^2 value that is $> 5\sigma$ away from the theoretical distribution, and sources with low signal-to-noise polarised emission resulting in artificially large values of $\sigma^2_{\rm RM}$ were flagged. This resulted in 196 bad fits out of 819 polarised sources. The following analysis is thus performed using the remaining 623 polarised radio sources detected in 124 galaxy clusters.

6.3 Methods

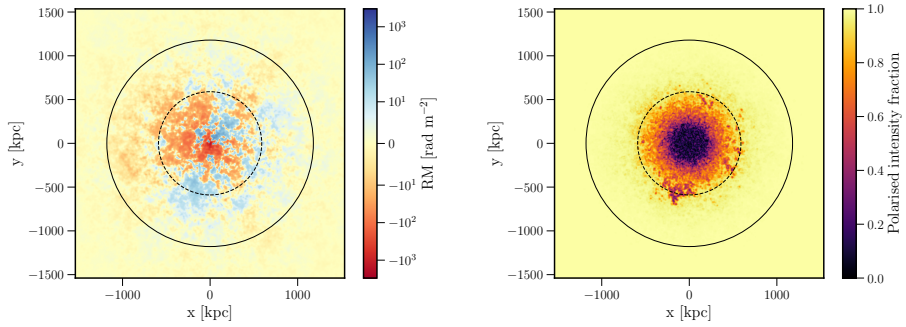

Figure 6.1: Simulated Faraday rotation (left) and depolarisation (right) screen for a random cluster from our sample as it would appear at 1.5 GHz with perfect sampling. The parameters are $B_0 = 5.0\,\mu$G, $n = 2$, $\eta = 0.5$ and the dashed and solid circles show $0.5R_{500}$ and $1.0R_{500}$, respectively.

The galactic contribution to the RM is expected to be small since the cluster sample is selected from the PSZ2 survey and thus avoids the galactic plane by design. While cluster induced RMs are often on the order of 10^3 rad m^{-2}, for comprehensiveness we subtracted the galactic contribution (on the order of 10^1 rad m^{-2}) to the sources using the recent map from Hutschenreuter et al. (2022), propagating the uncertainties as well. Afterwards, we corrected the RM to the cluster rest frame to account for cosmological redshift. This assumes that the RM, after subtraction of the galactic contribution, is dominated by the effect of the ICM and that the intrinsic RM of the source and the component from the intergalactic medium are both negligible in comparison. We thus defined the RM induced by the ICM as

$$\mathrm{RM}_{\rm cluster} = (\mathrm{RM}_{\rm obs} - \mathrm{RM}_{\rm gal})(1 + z_{\rm cluster})^2, \tag{6.3}$$

where $\mathrm{RM}_{\rm obs}$ refers to the best-fit RM in the observer frame, $\mathrm{RM}_{\rm gal}$ to the galactic contribution and $z_{\rm cluster}$ to the cluster redshift.

To infer magnetic field properties from the distribution of $RM_{cluster}$, we consider models of various levels of complexity. First, in the simple scenario of random magnetic field orientations in cells of size Λ_c kpc, which have uniform magnetic field strengths and electron densities, the observed RM is the result of a random walk process. Because of the central limit theorem, the distribution of RMs is then expected to be a Gaussian distribution with zero mean, and variance given by (e.g. Murgia et al., 2004)

$$\sigma^2_{\rm RM} = 812^2 \Lambda_c \int (n_e B_{\parallel})^2 dl, \tag{6.4}$$

where dl is the infinitesimal path length increment along the line of sight in kpc, n_e is measured in cm^{-3} and $B_{\parallel}$ is the magnetic field strength parallel to the line of sight in μG.

In reality, the magnetic field structure will more closely resemble a random field with fluctuations on many spatial scales, and both the magnetic field strength and electron density will scale with radius. Thus comparing observations to more realistic scenarios requires simulated magnetic fields. We followed the approach explained in Section 4 of Osinga et al. (2022) to generate mock rotation measure and depolarisation images for all clusters in our sample which have X-ray observations available (99/124). An example of a mock RM and depolarisation image is shown in Figure 6.1 for a random cluster in our sample. In these models, the magnetic field is assumed to be a three-dimensional Gaussian random field with a single-power law spectrum characterised by the following parameters: B_0, η, n, $\Lambda_{\rm min}$ and $\Lambda_{\rm max}$. The first two denote the variables that parameterise the magnetic field, assumed to follow (e.g. Bonafede et al., 2010)

$$B(r) = B_0 \left(\frac{n_{\rm th}(r)}{n_{\rm th}(0)} \right)^{\eta}, \tag{6.5}$$

and the last three parameters encode the power spectrum of the magnetic field:

$$|B_k|^2 \propto k^{-n}, \tag{6.6}$$

between minimum and maximum fluctuations scales that are denoted by $\Lambda_{\rm min}$ and $\Lambda_{\rm max}$ in image space, respectively. In the picture of Kolmogorov turbulence, $n = 11/3$, but this was found observationally to take values between $n = 1$ and $n = 4$ (Murgia et al., 2004; Govoni et al., 2006; Guidetti et al., 2008; Bonafede et al., 2010; Vacca et al., 2010, 2012; Govoni et al., 2017; Stuardi et al., 2021; Osinga et al., 2022). We have computed all models on 1024^3 pixel grids, to simulate all clusters in the same way. Here, one pixel represents 3 kpc, and clusters are thus simulated out to about $1.5R_{500}$, with a minimum fluctuation scale of $\Lambda_{\rm min} = 6$ kpc. These models will be compared to observations in various ways, as detailed in the next section.

6.4 Results

6.4.1 Average magnetic field strength

The cluster rotation measure with the uncertainty given by the 16th and 84th percentile of the MCMC is plotted as a function of distance to the nearest cluster centre in Figure 6.2. A clear trend is visible, with the scatter in the rotation measures decreasing with a

larger distance to the cluster centre. Taking all sources within $1.0R_{500}$, we find that the standard deviations of the RM of cluster members and background sources are similar[2], being 263 ± 56 and 216 ± 68 rad m^{-2}, respectively, as shown in Table 6.1. In reality, we expect that for a given magnetic field strength, the standard deviation of the RM of background sources is expected to be $\sqrt{2}$ times that of cluster members, as cluster members are on average located at the mid-plane of the cluster. However, cluster members are also found preferentially at smaller radii, where the scatter in RM is larger due to generally larger magnetic field strength and electron densities.

Table 6.1: Standard deviation of $\mathrm{RM_{cluster}}$ as defined in Eq. 6.3 for different subsets and projected radii.

	$< 0.5R_{500}$	$0.5 - 1.0R_{500}$	$< R_{500}$	$> R_{500}$
All	299 ± 61	120 ± 29	241 ± 44	38 ± 4
Inside[a]	288 ± 71	182 ± 48	263 ± 56	38 ± 7
Behind[b]	315 ± 103	57 ± 6	216 ± 68	37 ± 5
CC[c]	169 ± 67	85 ± 29	139 ± 49	27 ± 2
NCC[d]	236 ± 46	70 ± 9	192 ± 36	29 ± 6

Notes. [(a)] Sources located inside clusters [(b)] Sources located behind clusters [(c)] Only cool-core clusters [(d)] Only non-cool-core clusters

The mean value of the RMs is consistent with zero as a function of radius, as shown in Figure 6.3, consistent with random magnetic field orientations along the line of sight. Assuming the simple random walk scenario denoted by Equation 6.4, we find that the most rudimental estimate of the line-of-sight magnetic field strength is given by

$$\left(\frac{B_{\parallel}}{\mu G}\right) = 2.46 \left(\frac{\sigma_{\mathrm{RM}}/200}{\mathrm{rad\,m^{-2}}}\right) \left(\frac{n_e/10^{-3}}{\mathrm{cm^{-3}}}\right) \left(\frac{\Lambda_c/10}{\mathrm{kpc}}\right)^{-1/2} \left(\frac{L/1000}{\mathrm{kpc}}\right)^{-1/2} \tag{6.7}$$

where L indicates the line-of-sight column length, which will be on average twice as large for background sources as cluster members. If we assume that cells are ordered on scales of 10 kpc with an electron density of $10^{-3}\mathrm{cm}^{-3}$ (e.g. Böhringer et al., 2016), this reduces to

$$B_{\parallel} = \frac{\sigma_{\mathrm{RM}}}{2.57\ \sqrt{L}}. \tag{6.8}$$

If we assume approximately $L = 1000$ kpc for cluster members and twice as large for background sources, we find magnetic field strengths averaged within R_{500} equal to 2-3 μG. Although the simple scenario suffices to give an order of magnitude estimate for the average magnetic field in galaxy clusters, it is clear from Figure 6.2 that the product of the magnetic field strength and electron density is not constant as a function of radius.

To sample a more physical property, we plot in Figure 6.4 the observed rotation measures as a function of ICM electron column density. This plot is less populated, as we now only show sources that are detected within a projected radius $r < 2R_{500}$, where the Chandra-derived column density values are reliable. The increased scatter in rotation

[2]Uncertainties on σ_{RM} are calculated by 1 000 bootstraps.

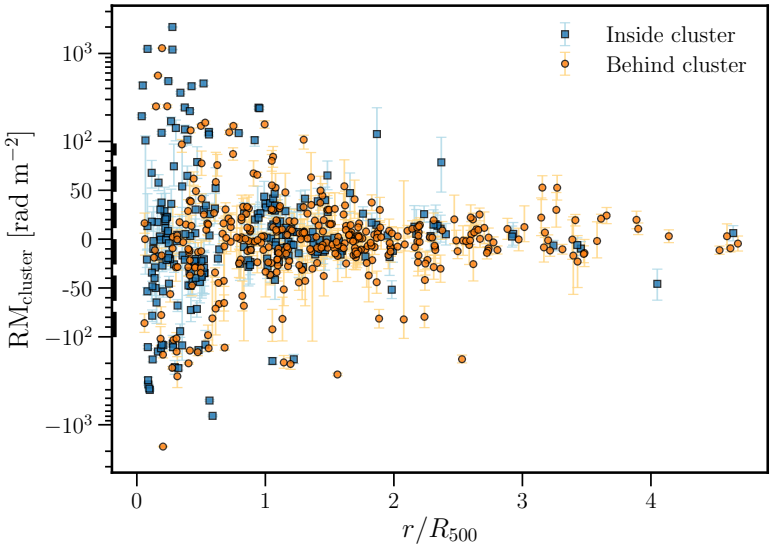

Figure 6.2: Cluster induced rotation measure as a function of normalised distance to the nearest cluster centre. The y-axis is partially linear and partially logarithmic for visibility. The region between -10^{-2} and 10^2 rad m^{-2}, indicated by the dashed axis, is shown on a linear scale and the scale is logarithmic outside of this region. The median uncertainty in RM is 13 and 11 rad m^{-2} in cluster members and background sources, respectively. The plot is shown on a linear scale in Appendix 6.6.

measure with increasing column density is still significant, and the preferential sampling of cluster members at high column densities (i.e. low radii) is clearly pronounced. Following Böhringer et al. (2016), we calculated the scatter in rotation measure in bins of column density, from which the average magnetic field strength along of the line of sight can be calculated as

$$\left(\frac{B_{\parallel}}{\mu G}\right) = 3.801 \times 10^{18} \left(\frac{\sigma_{\mathrm{RM}}}{\mathrm{rad\,m^{-2}}}\right) \left(\frac{N_e}{\mathrm{cm^{-2}}}\right) \left(\frac{L}{\Lambda_c}\right)^{1/2}. \tag{6.9}$$

The RM scatter as a function of column density is shown in Figure 6.5. The bottom panel of Figure 6.5 shows the resulting magnetic field estimate from Equation 6.9. We find that the average magnetic field strength is 0.3μG $\sqrt{L/\Lambda_c}$, resulting in around 3μG for typical values of $L = 1000$ kpc and $\Lambda_c = 10$ kpc (Böhringer et al., 2016). There is a hint of increasing average magnetic field strength towards lower column densities, although this is likely dominated by the scatter from the uncertainties in the RM, as will be discussed in the next section.

6.4.2 Radially declining magnetic field

In reality, cluster magnetic fields and electron densities show a radial decline. To investigate the (spherically averaged) magnetic field properties as a function of radius, we calculated the scatter in rotation measure as a function of radius. The data were binned into radial

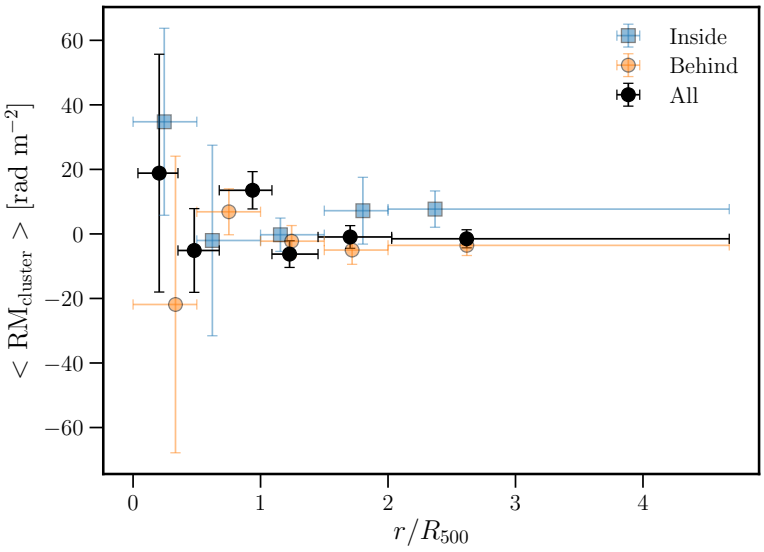

Figure 6.3: Mean of the cluster induced rotation measure in bins of projected normalised distance to the nearest cluster centre. The horizontal error bars indicate the bin edges. Cluster members are shown in blue, background sources in orange, and the combined bins in black.

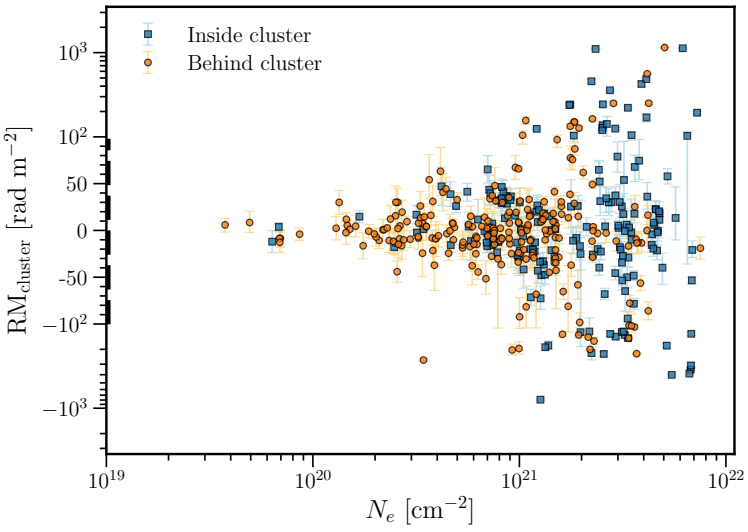

Figure 6.4: Cluster induced rotation measure as a function of electron column density, for sources detected at $r < 2R_{500}$. The y-axis is partially linear and partially logarithmic for visibility. The region between -10^{-2} and 10^2 rad m^{-2}, indicated by the dashed axis, is shown on a linear scale and the scale is logarithmic outside of this region. The plot is shown on a linear scale in Appendix 6.6.

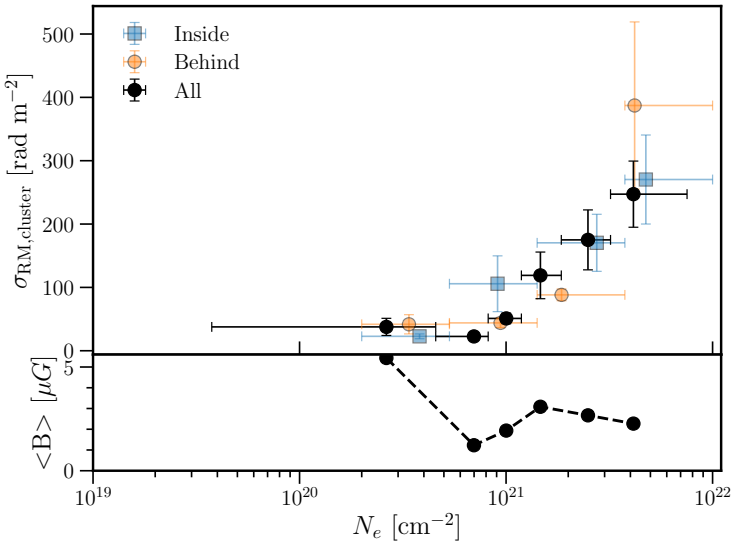

Figure 6.5: Standard deviation of the RMs in bins of electron column density, for sources detected at $r < 2R_{500}$. The bins for the full sample have equal frequency with 70 sources per bin, while the bins for the sub-samples are defined in logarithmically spaced bins to sample similar densities. The horizontal error bars indicate the bins, and points are plotted at the median N_e. The bottom panel shows the magnetic field estimate assuming Equation 6.9, with a correlation length that is a factor 100 smaller than the line-of-sight distance, resulting in a mean strength of 3μG.

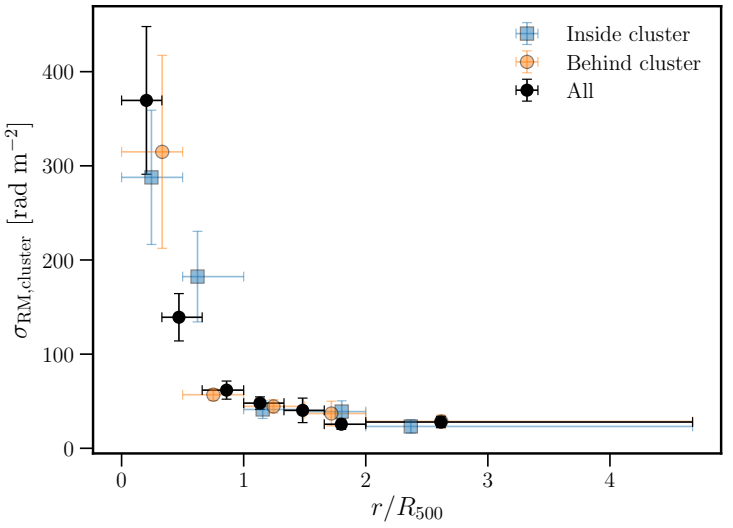

Figure 6.6: Standard deviation of the RMs in bins of projected distance to the nearest cluster centre. The horizontal error bar indicates the width of the bin, and the points are plotted at the median radius in the bin.

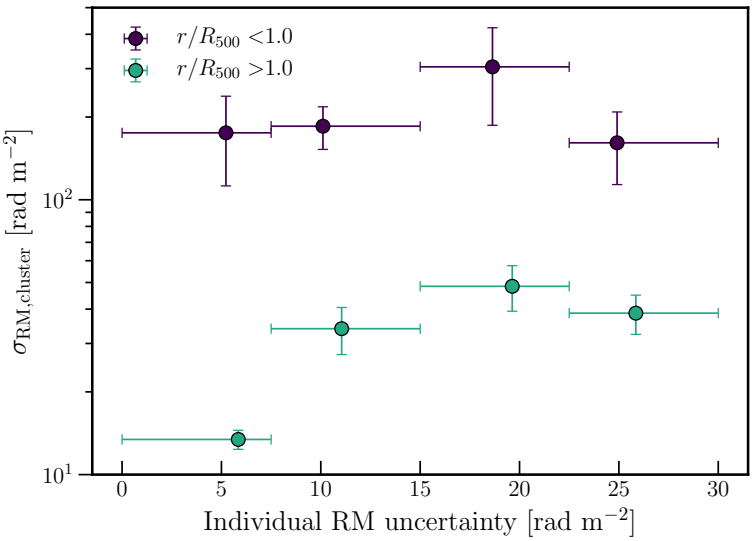

Figure 6.7: Scatter in rotation measure as a function of the RM uncertainty, separately for sources detected within R_{500} and outside R_{500}.

bins, and the standard deviation is shown as a function of radius in Figure 6.6. A strong trend of the RM scatter being significantly higher closer to the cluster centre is present.

The RM scatter at large radii (i.e. $r > 2R_{500}$) is still considerably above zero, with a value of $\sigma_{\mathrm{RM}} = 28 \pm 6$. It is likely that this value reflects the uncertainties in the RM determination. To verify this, we plot in Figure 6.7 the scatter σ_{RM} as a function of the individual RM uncertainty. The plot shows that the scatter outside $1R_{500}$ is already dominated by the uncertainties, with the observed σ_{RM} increasing with the RM uncertainty. For sources located within $1R_{500}$, we see no such trend, indicating that the scatter is dominated by the real physical scatter induced by the turbulent magnetic medium. However, the RM scatter near the centre of the clusters is likely underestimated, as sources with large RM values are depolarised, given that the 50% sensitivity Faraday depth is equal to only 1200 rad m^{-2} for the channel width of our observations (Osinga et al., 2022).

Assuming that the magnetic field fluctuates on a single scale Λ_c regardless of radius, we can determine the magnitude of the 3D magnetic field fluctuations and the scaling between magnetic field and thermal electron density from the σ_{RM} profile. In this assumption, the variance in rotation measure as a function of projected distance is proportional to the line-of-sight integral of Equation 6.4,

$$\sigma^2_{\mathrm{RM}}(r/R_{500}) = \sigma_{\mathrm{RM,0}} \int_{\mathrm{LOS}} n_e^{2(1+\eta)}(\mathbf{r})\,\mathrm{d}L, \tag{6.10}$$

where $\sigma_{\mathrm{RM,0}}$ denotes the theoretical central RM dispersion and η models the relationship between the magnetic field energy density and thermal energy density (i.e. $B^2 \propto n_e^{2\eta}$),

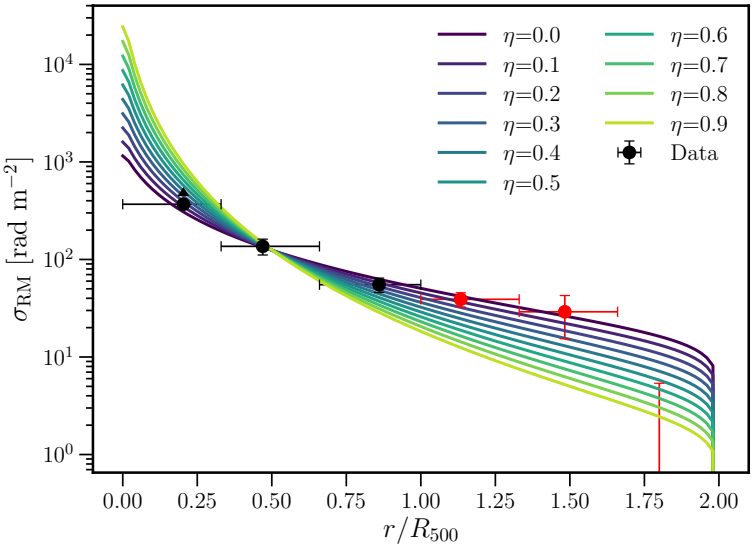

Figure 6.8: RM scatter as a function of projected distance. The data is corrected for a baseline value of $\sigma_{\rm RM} = 28$, meaning the last data point is consistent with zero. The first point is plotted as a lower limit, and points outside R_{500} (shown in red) are ignored in the fit, as Fig. 6.7 showed that the scatter is dominated by uncertainties for these points. The coloured lines show best-fit profiles computed for various values of η assuming Equation 6.10.

which was found to be 0.5 in the Coma Cluster (e.g. Bonafede et al., 2010). Because we are investigating a stacked sample of clusters this scaling might, in reality, be more complicated, but this can only be investigated in single clusters with next-generation polarisation data. At the moment, we determined an average cluster electron density profile by stacking all individual profiles, which are shown in Figure 6.19, which is on average a good assumption because clusters are relatively self-similar (e.g. Arnaud et al., 2010a).

Correcting for the scatter from measurement uncertainties, we compare in Figure 6.8 the observed RM scatter with the theoretical profile from integrating the mean density profile along the line-of-sight out to $2R_{500}$ for various values of η. This figure demonstrates that the observed RM scatter profile is relatively flat, with models requiring $\eta \leq 0.5$ to fit the observed RM scatter observed in the centre of clusters. The best-fit parameters are found to be $\sigma_{\rm RM,0} = 1538$ rad m^{-2} and $\eta = 0.15$, but we note that this value of eta likely presents a lower limit, because the observed RM scatter at small projected radii is a lower limit, as explained more in Section 6.5.

If we fit a β-model to the cluster density profile, we can de-project the profile and calculate the 3D central magnetic field dispersion $\sigma_{B,0}$ as (e.g. Johnson et al., 2020)

$$\sigma_{B,0} = \sigma_{\rm RM,0} \frac{\sqrt{3}}{812\,\pi^{1/4}}\, n_0^{-1}\, \Lambda_0^{-1/2}\, r_c^{-1/2} \sqrt{\frac{\Gamma(\alpha_1 + 1/2)}{\Gamma(\alpha_1)}}. \tag{6.11}$$

where Λ_0 is the unknown characteristic length scale of the magnetic field and $\alpha_1 = \frac{3}{2}(1+$

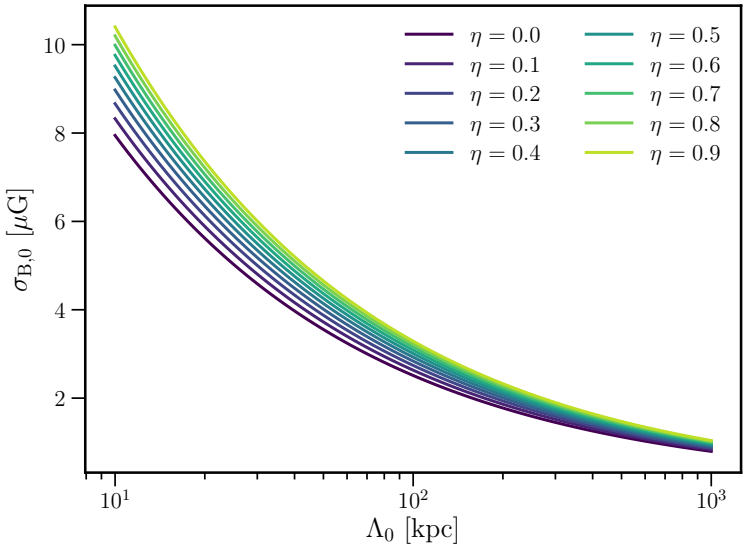

Figure 6.9: Central magnetic field dispersion, calculated from Eq. 6.11, as a function of the characteristic length scale Λ_0 and the magnetic field to thermal electron density scaling parameter η.

$\eta)\beta_c - \frac{1}{4}$. Figure 6.9 shows the value of $\sigma_{B,0}$ against Λ_0. For a reference value of $\Lambda_0 = 10$ kpc and $\eta = 0.15$, we find that $\sigma_{B,0} = 8\,\mu$G.

6.4.3 Cluster members vs background sources

Theoretically, since cluster members are on average located at the midplane of the cluster and polarised light thus travels through half the column that background sources probe, we would expect background sources to display a scatter in RM that is on average greater by a factor $\sqrt{2}$. However, from Figure 6.6 it becomes clear that such an effect is not observed. To investigate this in more detail, we calculated a more robust measure of scatter, the interquartile range. This is defined as the difference between the 75th and 25 percentiles of the data such that a few sources with large RM values do not dominate the scatter. The interquartile range is shown in Figure 6.10. The trend of increasing scatter with decreasing radius is still visible, but cluster members and background sources show similar scatter even when computed at similar radii.

To quantify this, we performed a z-test to test two null hypotheses in every bin: i) that the scatter of background sources and cluster members are the same, and ii) that the scatter of background sources is $\sqrt{2}$ times the scatter of cluster members. We found that we could reject neither of the null hypotheses with 95% confidence. This implies that the uncertainties are currently still too large to identify a statistically significant difference between the RM of background sources and cluster members. To increase the number statistics, we also tried binning all sources into a radial bin bounded by $[0, R_{500}]$, and found marginal evidence ($p = 0.02$) to reject the null hypothesis that $\mathrm{IQR}(\mathrm{RM}_{\mathrm{behind}}) = \sqrt{2}\cdot\mathrm{IQR}(\mathrm{RM}_{\mathrm{inside}})$. However,

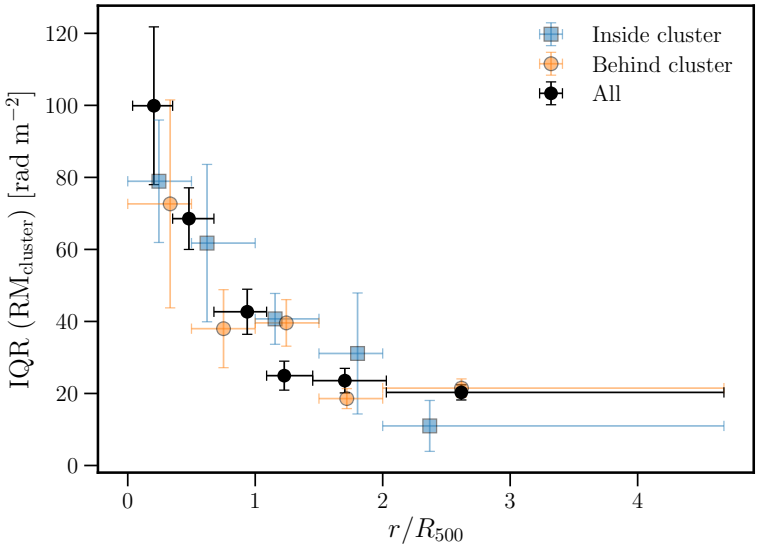

Figure 6.10: Interquartile range of the RMs in bins of projected distance to the nearest cluster centre. The bins for the full sample have equal frequency with 98 sources per bin, while the bins for the subsamples are defined in steps of $0.5R_{500}$ up to $2R_{500}$ to sample similar radii. The horizontal error bar indicates the width of the bin, and the points are plotted at the median radius in the bin. Uncertainties are calculated from 1 000 bootstraps.

this is likely caused by the fact that the cluster members are preferentially detected at smaller radii (median radius $0.34R_{500}$) than background sources (median radius $0.54R_{500}$), where the scatter is expected to be larger.

6.4.4 Merging vs relaxed clusters

Differences between the magnetic fields of relaxed and merging clusters have been tentatively observed in various studies (Bonafede et al., 2010; Stasyszyn & de los Rios, 2019; Osinga et al., 2022), but not yet clearly quantified. Following Osinga et al. (2022), we split our sample into merging and relaxed clusters based on the presence of a cool-core (CC) or absence of one (NCC). We defined the same bins as Osinga et al. (2022) to separate the central cooling core region ($r < 0.2R500$), as this is where the enhanced electron density of the cool-core clusters becomes noticeable, as also shown in Figure 6.19. The scatter in RM as a function of distance for the NCC and CC clusters is shown in Figure 6.11. We note that the central bin only has 7 sources in the CC sample (while the NCC sample has 37), which prevents using the IQR as a robust estimate of the scatter. There is a hint that CC clusters have higher $\sigma_{\rm RM}$ as expected from the increased electron density in the cooling core region, but the uncertainties are too large to reliably conclude such an effect. We do however see that merging clusters have significantly higher RM scatter in the region $0.2 < r/R_{500} < 1.0$ where 90 and 88 sources are detected respectively in both sub-samples.

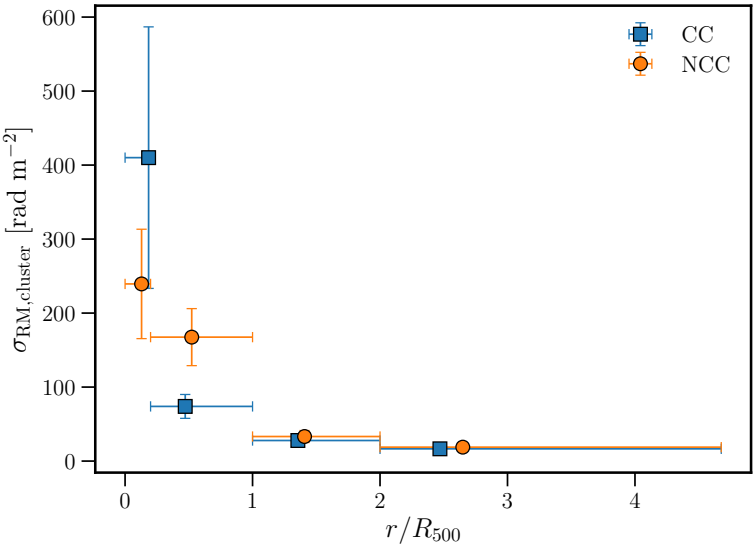

Figure 6.11: Standard deviation of RM as a function of projected distance to the nearest cluster centre, separately for CC and NCC clusters. The horizontal error bar indicates the width of the bin, and the points are plotted at the median radius in the bin.

6.4.5 Comparison to models

To compare the data to more involved models with a radial decline of magnetic field values and electron densities determined per cluster, and a power spectrum of magnetic field fluctuation scales, we follow the principle as laid out in Section 6.3, simulating magnetic fields with a 1024^3 pixel grid with a pixel size of 3 kpc. In the following section, we thus consider only sources that are detected at $\lesssim 1500$ kpc. This results in 303 polarised radio sources detected in 70 clusters for which X-ray information is available and simulations could be evaluated.

Constraining the magnetic field power spectrum

Both the RM and depolarisation of sources scale similarly (although not identically) with the magnetic field strength, but differently with n and Λ_{max}, and therefore the ratio can be used to constrain n and Λ_{max}, relatively independent of the other parameters (e.g. Bonafede et al., 2010). We defined the RM ratio as

$$\mathrm{RM\,ratio} = \frac{|\mathrm{RM}|}{1 - DP}. \tag{6.12}$$

This ratio is also relatively independent of radial distance, as the depolarisation will increase (i.e. take lower values of DP) as the RM increases towards the cluster centre. We verified this with both Spearman and Pearson tests, which showed no significant correlation.

The median observed RM ratio across all sources was found to be 139 ± 17, with the uncertainty calculated by 1 000 bootstraps. Figure 6.12 shows the median observed RM ratio

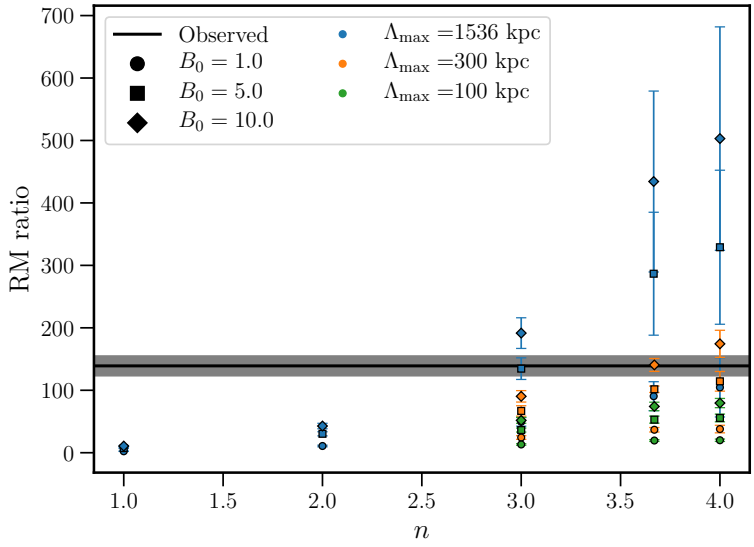

Figure 6.12: RM ratio, as defined in Equation 6.12, as a function of magnetic field power spectrum index n. The median observed value is indicated by the black line, while the simulated values are indicated by the coloured points, with different markers for different magnetic field strengths. The uncertainty on the simulated values reflect the 16th and 84th percentile of 10 random initialisations.

compared with simulated values for sources sampled at similar positions in the simulated RM and depolarisation images. It is clear from the figure that models with most of the magnetic field energy on small scales (i.e. $n < 3$) cannot reproduce the observed RM ratio, mainly because those models result in too low values of |RM| due to the rapidly fluctuating magnetic field along the line of sight. Instead, models with $n \geq 3$ provide a good fit for various values of the maximum correlation scale Λ_{max}. Lowering Λ_{max} has an analogous effect to lowering n, namely decreasing the coherence length of the magnetic field along the line of sight. This thus results in a smaller average |RM| while the effect on depolarisation is less significant, as this is measured on scales below the observing beam (less than typically 15 kpc, although dependent on cluster redshift). Thus, the observed data best matches $n \geq 3$.

For a Kolmogorov spectrum ($n = 3.67$) with typical values of the central magnetic field strength between $1 - 10\,\mu$G, the data is consistent with $\Lambda_{max} > 300$ kpc. Lower values of Λ_{max} would require significantly higher central magnetic field strengths.

Constraining the maximum correlation scale

To attempt to constrain the maximum projected correlation scale of the magnetic field, we computed the RM structure function[3]. The structure function is sensitive to fluctuations in rotation measure on varying scales. If the thermal electron density and magnetic field

[3]The structure function was computed using the framework from `https://github.com/AlecThomson/structurefunction`

strength are uniform, the structure function can be used to infer the power spectrum of the magnetic field (Ensslin et al., 2003). Although this is not the case across our cluster sample, the structure function is still a useful estimate to characterise RM fluctuations as a function of physical scales.

The (two point) structure function is defined as (e.g. Haverkorn et al., 2004)

$$\mathrm{SF}_{\mathrm{RM,obs}}(\Delta r) = \langle \mathrm{RM}(\mathbf{x}) - \mathrm{RM}(\mathbf{x}+\mathbf{r}) \rangle \,. \tag{6.13}$$

where the average is taken over all pairs at positions $\mathbf{x}$ and $\mathbf{x}+\mathbf{r}$ with similar distance Δr between the two components. Taking into account the offset added by the uncertainties on the RM, we computed the corrected structure function as

$$\mathrm{SF}_{\mathrm{RM}}(\Delta r) = \mathrm{SF}_{\mathrm{RM,obs}}(\Delta r) - \mathrm{SF}_{\sigma_{\mathrm{RM}}}(\Delta r), \tag{6.14}$$

where $\mathrm{SF}_{\sigma_{\mathrm{RM}}}$ denotes the offset correction, calculated by computing the structure function of the uncertainties. This correction was found to be on the order of $< 10\%$ of the observed structure function, as is shown in Figure 6.20.

The uncertainty on the observed structure function was computed numerically by bootstrapping the catalogue 100 times. Because we are interested in the structure function of the cluster magnetic field and not that of the intrinsic radio sources, we computed the projected distance between the radio source pairs by placing them at the cluster redshift, as that is the location of the Faraday screen. This assumes that the intrinsic RMs of source pairs are uncorrelated, which is a good assumption since they are almost exclusively unrelated sources. However, the fact that sources in a similar Δr bin can be located at different radial distances complicates the interpretation of the structure function, unless the form of the power spectrum is independent of radius, and only the amplitude scaling is affected.

The structure function is expected to approach zero for small values of Δr and $2\sigma^2_{\mathrm{RM}}$ for large values of Δr (Haverkorn et al., 2004; Johnson et al., 2020). In the Gaussian random field assumption, the amplitude of the structure function scales with B^2, because the scatter in RM scales linearly with B. We thus plot normalised structure functions, as we are not interested in the B^2 normalisation in this section.

The structure function is shown in Figure 6.13a, where the distance between pairs is normalised by the host cluster R_{500} to stack different clusters together and only sources detected at $r < R_{500}$ were used. The form of the structure function is relatively flat, showing no clear increase as a function of projected separation, indicating that it has already saturated. This would mean that the characteristic scale of RM fluctuations is below $0.05R_{500}$, or roughly 50 kpc. However, when we compare the observed structure function to the structure function calculated from simulated RM images with an equivalent sampling of sight lines, the simulated structure functions all show similar behaviour to the observed structure function, indicating the radial location of the sightline is dominating the form of the structure function. This is clearly seen when sources are not sampled at equivalent positions, as shown in Figure 6.13b. This means that current data do not allow us to distinguish different characteristic correlation scales through the structure function.

We can, however, compute the structure function in bins of projected radius, to investigate whether the magnetic field adheres to a similar power spectrum as a function of projected radius. The structure function computed in three different radial bins is shown

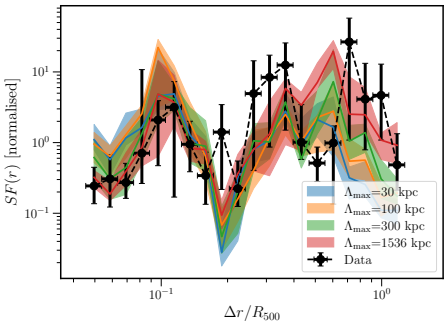

(a) Sampled at an equal number of equivalent sightlines.

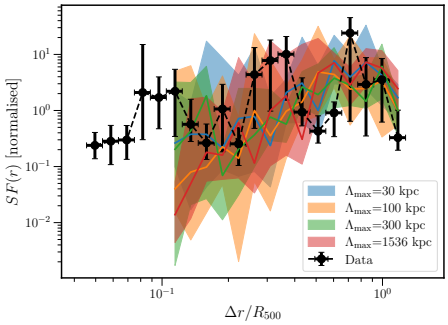

(b) Sampled at an equal number of randomly placed sightlines. Bins at small separations are now omitted as not enough source pairs were found in the simulations.

Figure 6.13: RM structure function as a function of normalised pair separation in 20 logarithmically spaced bins. The black points indicate the observed values, while the coloured points indicate simulated values for a Kolmogorov power spectrum. All functions are normalised to have a median amplitude equal to 1, as the amplitude is degenerate with B_0^2. The shaded regions show the 16th and 84th percentiles of 10 random initialisations.

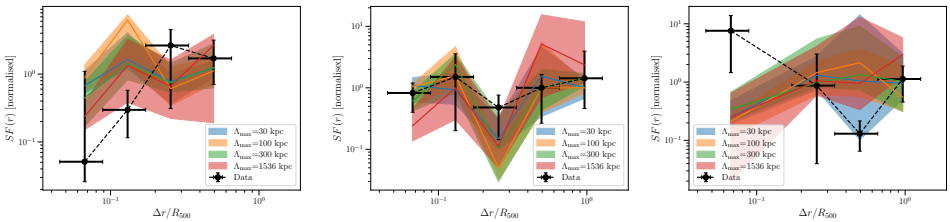

(a) $0.0 < r/R_{500} < 0.33$ (b) $0.33 < r/R_{500} < 0.66$ (c) $0.66 < r/R_{500} < 1.0$

Figure 6.14: Equivalent to Fig. 6.13a, but in bins of projected distance.

in Figure 6.14. From this figure, we see that the observed structure function is consistent with being constant for all three radial bins. We thus find no evidence that the structure of the magnetic field is different as a function of radius.

Full forward model

Finally, we find the best model that reproduces the data by following the approach used in previous works such as Murgia et al. (2004); Bonafede et al. (2010); Govoni et al. (2017); Stuardi et al. (2021), directly comparing the simulated RM and depolarisation images to the observed data. For every source, we sample an equivalent source from the simulated clusters, and compute the expected RM and depolarisation. We minimize the difference between the simulated and observed radial scatter in RMs, and the depolarisation as a

function of radius. We define the function to be minimized, q, as follows

$$q = q_{\rm depol} + q_{\rm RM} = \sum_r \left(\frac{{\rm DP}_{\rm obs}(r) - \langle {\rm DP}_{\rm sim}(r) \rangle}{{\rm err}({\rm DP}_{\rm obs})} \right)^2 + \left(\frac{\sigma_{\rm RM,obs}(r) - \langle \sigma_{\rm RM,sim}(r) \rangle}{{\rm err}(\sigma_{\rm RM,obs})} \right)^2, \quad (6.15)$$

where the observables are calculated in bins of projected radii (equivalent to Fig. 6.6), and the simulated observables, denoted by the angle brackets, are averaged over 10 different random initialisations. Because sources in this sample were found to be intrinsically depolarised with DP=0.92 at large radii (Osinga et al., 2022), we incorporated this into the simulated depolarisation. Similarly, we correct $\sigma_{\rm RM}$ for the contribution caused by the uncertainties by subtracting in quadrature the observed $\sigma_{\rm RM}$ in the last bin from the $\sigma_{\rm RM}$ profile. As Section 6.4.5 showed that the RM ratio is consistent only with models that have $n > 3$, we fix the power spectrum to the Kolmogorov value of $n = 3.67$ to reduce the computational burden.

First, we investigate the best-fit models when fixing the magnetic field to electron density scaling to the typical value of $\eta = 0.5$. Figures 6.15a and 6.15b show the values of $q_{\rm depol}$ and $q_{\rm RM}$ respectively, as a function of B_0 and $\Lambda_{\rm max}$. We find the best agreement for a model with $B_0 = 5.0\,\mu$G and a maximum correlation scale equal to either $\Lambda_{\rm max} = 1536$ kpc or $\Lambda_{\rm max} = 300$ kpc. These models have very similar total q values, but $\Lambda_{\rm max} = 1536$ kpc is preferred by the depolarisation profile, while $\Lambda_{\rm max} = 300$ kpc is preferred by the $\sigma_{\rm RM}$ profile. The measured and simulated radial profiles are shown in Figure 6.16 for both best-fit models. Both models ($\Lambda_{\rm max} = 300$ and 1536 kpc) are shown to fit the data very well, although the observed $\sigma_{\rm RM}$ at a low projected radius is in both cases lower than the simulated value. This is likely due to the selection effect that sources with high values of RM will be depolarised and thus missed, biasing our observed $\sigma_{\rm RM}$ low, as discussed more in the next section. This selection bias is less important for radial depolarisation because upper limits on DP can be calculated from unpolarised sources as well.

Section 6.4.2 showed that the radial profile of $\sigma_{\rm RM}$ preferred low values of $\eta \approx 0.1$. We thus also test the value of $\eta = 0.1$, although we stress again that this might be caused by missing preferably high RM sources at low radii. The plots are shown in Appendix 6.6, Figures 6.21 and 6.22. The modelled $\sigma_{\rm RM}$ curve does provide a better fit for $B_0 = 1.0\mu$G, $\Lambda_{\rm max} = 300$ kpc and $\eta = 0.1$, although the model now underestimates the central scatter, while in reality, the central scatter is likely higher than what we observed. Additionally, the depolarisation profile shows a worse fit to the data for this model, instead favouring $B_0 = 10\,\mu$G and $\Lambda_{\rm max} = 30$ kpc, which is rejected on the basis of the RM ratio analysis in Section 6.4.5. A model with $\eta = 0.5$ thus better explains both the depolarisation and RM scatter profile simultaneously.

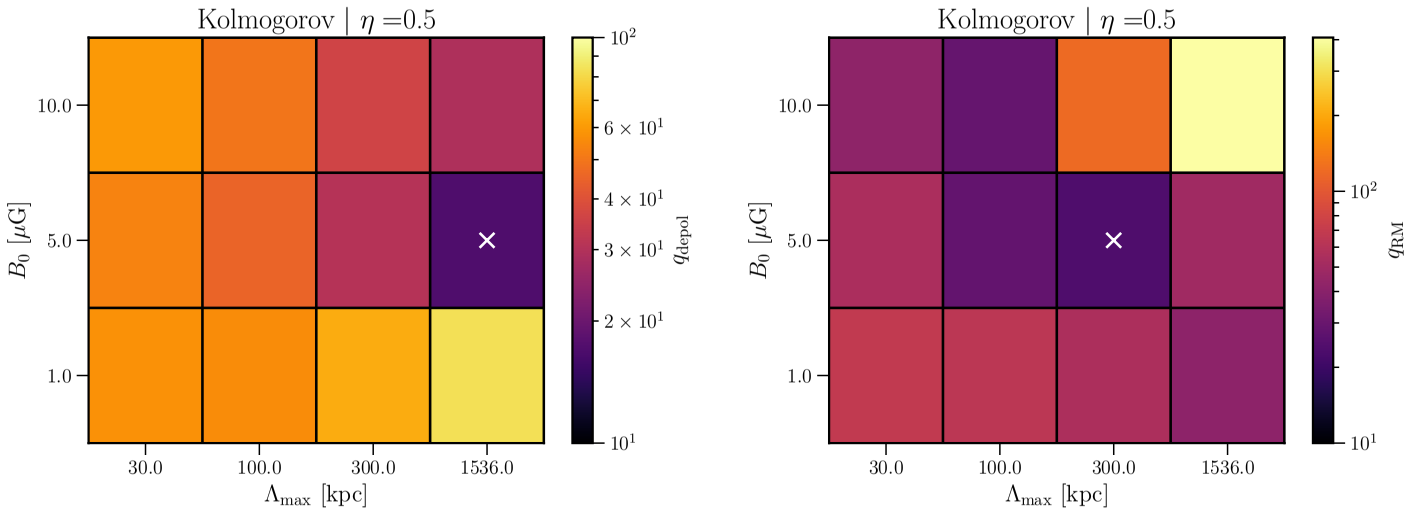

(a) (b)

Figure 6.15: Values of q_{depol} (a) and q_{RM} (b) as defined in Equation 6.15 for combinations of B_0 and Λ_{RM}. Models are simulated with a Kolmogorov power spectrum and $\eta = 0.5$. The best-fit model is marked by a cross.

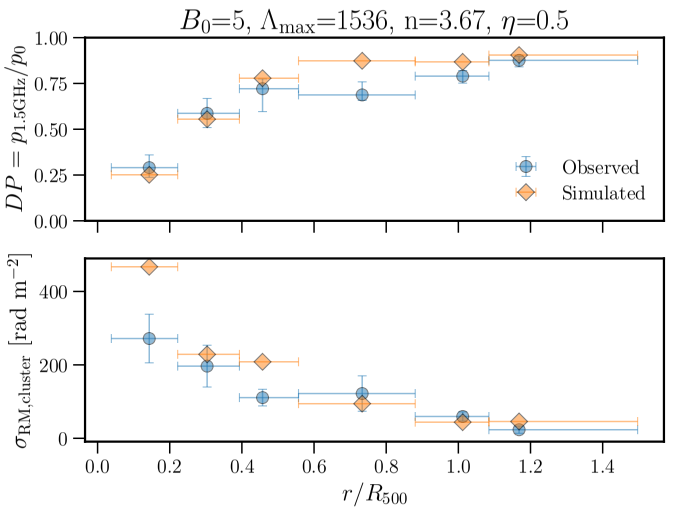

(a) Model that minimizes q_{depol}.

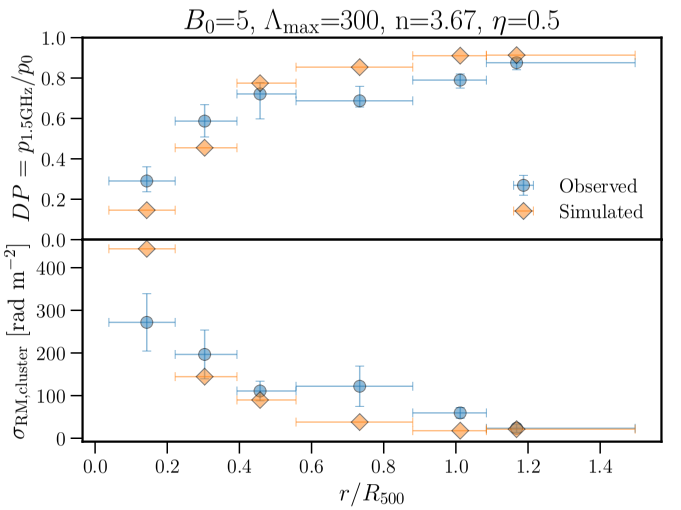

(b) Model that minimizes q_{RM}.

Figure 6.16: Comparison between observed and forward-simulated depolarisation and RM scatter for two models that minimize the q statistic as defined in Equation 6.15.

6.5 Discussion

Previous studies of samples of clusters have investigated either the statistical depolarisation (Bonafede et al., 2010; Osinga et al., 2022) or the rotation measure as a function of projected radius (Clarke et al., 2001; Böhringer et al., 2016; Stasyszyn & de los Rios, 2019). In this work, we have for the first time measured both the rotation measure and depolarisation in a consistent way for polarised radio sources along sight-lines of stacked galaxy clusters.

The previously largest statistical study was performed by Böhringer et al. (2016), who found 92 RM sight-lines within R_{500} by cross-matching 1773 clusters with the RM catalogue compiled by Kronberg & Newton-McGee (2011). We significantly increase the number statistics, detecting 261 radio sources with well-defined RM and depolarisation within R_{500} in only 124 clusters. Comparing Table 6.1 with Table 1 in Böhringer et al. (2016), we find significantly higher $\sigma_{\rm RM}$ in all radial bins, except outside R_{500}. The reason for this is likely twofold. First, there is a difference in the RM sensitivity as the Böhringer et al. (2016) is likely based on radio data with larger channel widths, preventing detection of high RMs (they find a maximum $|{\rm RM}| < 700$ rad m^{-2}). Second, the cluster samples are different, as Böhringer et al. (2016) quote a mean cluster mass of $3\times10^{14} M_{\odot}$, while only 15 out of our 124 clusters have a mass below this value, and the mean mass of our sample is $5.7\times10^{14} M_{\odot}$. Taking the different sampling into account by calculating the scatter as a function of electron column density in Section 6.4.1, we found an average magnetic field estimate of $3\,\mu$G in our sample of galaxy clusters, perfectly consistent with the findings of Böhringer et al. (2016).

The observed scatter of RMs was found to be dominated by the effect of the ICM inside R_{500}, but dominated by the uncertainties in the RM outside R_{500}, as shown in Figure 6.7. At large radii (i.e. $r > 2R_{500}$) we observed $\sigma_{\rm RM} = 28 \pm 6$, which is a combination of source to source RM scatter and measurement uncertainties. This is lower than the value of 56 ± 8 found by Böhringer et al. (2016), but significantly higher than the expected intrinsic variation in the radio sources of $5-7$ rad m^{-2} (Schnitzeler, 2010). We thus cannot determine the magnetic field properties on the outskirts of galaxy clusters, as we are dominated by the uncertainties in the RM determination. However, inside R_{500}, the radial profile of the scatter can be used to determine the magnetic field strength and radial profile, as shown in Figure 6.8.

The RM scatter inside R_{500} showed a flat radial profile compared to expectations from a simple scaling of the magnetic field with the electron density of clusters. Plasma theories generally predict $\eta > 0.5$, with flux freezing giving $\eta = \frac{2}{3}$, adiabatic compression giving $\eta = 1.0$ and dynamo models often predicting a constant magnetic energy density to thermal energy density ratio (i.e. $\eta = 0.5$). Observationally, the best determined magnetic field profile is that of the Coma cluster, for which $\eta = 0.4-0.7$ was found. Other studies using resolved (cluster) radio galaxies also find $\eta \geq 0.5$ (Murgia et al., 2004; Vacca et al., 2012; Govoni et al., 2017; Stuardi et al., 2021). In comparison, we found that the best-fit $\sigma_{\rm RM}(r)$ model preferred $\eta > 0.15$, which is below the other experimental and theoretical values. However, statistical studies such as this one that use RMs of unresolved radio sources to determine the RM scatter suffer from a significant observational bias as sources with high RM values near the centre of clusters are likely to be depolarised and thus missed. The observed electron density profiles, shown in Fig 6.19, illustrate the problem as the electron densities rise strongly towards the core of clusters. Using Eq. 6.10, we expect $\sigma_{\rm RM}$ to be

$\sim$ 10 times larger at $r = 0.25R_{500}$ than at $r = 0.5R_{500}$. Since the scatter observed at $0.5R_{500}$ is on the order of 10^2 rad m^{-2}, we expect a scatter on the order of 10^3 rad m^{-2} at $r = 0.25R_{500}$. Sources with such high RM scatter are quickly depolarised at L-band frequencies (Osinga et al., 2022), presenting a missing data problem. This artificially decreases the steepness of the $\sigma_{\rm RM}$ profile, requiring low values of η to match the data. In contrast, studies relying on resolved radio sources often probe $\sigma_{\rm RM}$ on smaller scales (i.e. the size of the radio source) where fluctuations are expected to be significantly smaller and thus if a polarised radio source is detected, the scatter can be determined more accurately (e.g. Bonafede et al., 2010).

Other statistical studies probing many unresolved sightlines such as Böhringer et al. (2016); Stasyszyn & de los Rios (2019) have also not observed a strong increase of $\sigma_{\rm RM}$ at low radii, implying the same observational bias. However, at higher frequencies, RM values as high as 10,000 have been observed in the centre of some clusters (e.g. Taylor & Perley, 1993). Higher frequency data that suffers less from depolarisation is thus needed to determine the value of η accurately, but the current value $\eta > 0.15$ can be interpreted as a lower limit.

Depolarisation does not suffer as strongly from this observational bias at low radii, as upper limits on depolarisation fractions can still be set on sources that are significantly depolarised. Thus, we finally fit both the $\sigma_{\rm RM}$ and depolarisation radial profile jointly by means of forward modelling. When fixing the magnetic field to electron density scaling to the observationally best-determined value of $\eta = 0.5$ (Bonafede et al., 2011). The best-fit model was found to have $B_0 = 5.0\mu$G and $\Lambda_{\rm max} \geq 300$ kpc. The central magnetic field strength is consistent with previous single object studies as well as statistical studies (Murgia et al., 2004; Govoni et al., 2006; Guidetti et al., 2008; Bonafede et al., 2010; Vacca et al., 2010, 2012; Govoni et al., 2017; Stuardi et al., 2021; Böhringer et al., 2016). However, the correlation scale is significantly larger than found in resolved cluster member studies that typically find values around 50 kpc (Guidetti et al., 2008; Bonafede et al., 2010; Vacca et al., 2012; Govoni et al., 2017), although the resolved sources are often limited in size to less than a few hundred kiloparsec. Studies that use the brightness fluctuations or possibly polarised emission of radio halos to constrain the magnetic field power spectrum found results consistent with outer magnetic field fluctuation scales of $\sim$ 400kpc (Govoni et al., 2005; Vacca et al., 2010), agreeing with our estimate. Fluctuations on scales of more than a few hundred kpc are also expected theoretically, as the turbulent dynamo process thought to be responsible for magnetic field amplification in galaxy clusters is expected to occur on various scales, from less than a kpc up to a Mpc (Donnert et al., 2018).

In our modelling, we have decided to combine the information from cluster members and background sources, as Osinga et al. (2022) showed that the depolarisation properties of cluster members and background sources were similar. We checked for a local contribution to $\sigma_{\rm RM}$ from cluster members in Section 6.4.3 but found that we could reject neither the null hypothesis that cluster members and background sources have similar scatter nor the null hypothesis that background sources show a scatter that is $\sqrt{2}$ times larger. This is in accordance with the interpretation from Osinga et al. (2022) that, at the moment, we do not have the number statistics to confidently assert that cluster members are a biased probe of the magnetised ICM.

Finally, we checked for qualitative differences between merging and relaxed clusters.

During cluster mergers, turbulence is injected on large scales, which can amplify magnetic fields, and drive large fluctuation scales (e.g. Vacca et al., 2018). Relaxed clusters, on the other hand, are expected to have smaller fluctuation scales, as the energy injected by a previous merger has dissipated through cascades to smaller and smaller scales. We found that merging clusters show higher values of $\sigma_{\rm RM}$ in the region $0.2 < r/R_{500}$, while relaxed clusters tentatively showed larger scatter inside the dense cooling core region (Fig. 6.11). The higher RM scatter in merging clusters was also observed by Stasyszyn & de los Rios (2019), although with larger radial bin sizes. If a scaling between B and n_e is assumed, then CC clusters would indeed show a steep radial profile in both $\sigma_{\rm RM}$ and depolarisation (which was observed in also in Osinga et al. 2022), while NCC clusters should show a flatter profile, as the thermal gas density follows a flatter profile. The observed difference between the radial RM scatter in CC and NCC clusters is thus consistent with the behaviour of the thermal plasma in galaxy clusters.

6.6 Conclusion

This work has presented the continuation of the study presented in Osinga et al. (2022), where VLA L-band polarisation observations of 124 massive Planck clusters were presented, and the depolarisation properties of polarised sources were investigated as a function of radius. We have incorporated the additional information from the best-fit RM and constrained cluster magnetic field properties by combining depolarisation and RM in a sample of clusters for the first time. We summarise the results of this work as follows:

1. We have clearly detected the increase of the scatter in rotation measure as a function of decreasing projected radius or increasing electron column density. Averaging all 124 clusters, we find a scatter within R_{500} of $\sigma_{\rm RM} = 241 \pm 44$ rad m^{-2}. The scatter outside of R_{500} was found to be 38 ± 4 rad m^{-2} and dominated by the uncertainties in the RM determination.

2. Assuming that magnetic fields fluctuate on a single characteristic length scale Λ_c with a constant strength, the observed RM scatter agrees with an average magnetic field strength within R_{500} of $3\,(\Lambda_c/10{\rm kpc})^{-0.5}\,\mu$G.

3. The profile of $\sigma_{\rm RM}$ as a function of projected radius requires a scaling of $B \propto n_e^{\eta}$ with $\eta > 0.15$. This value presents a lower limit, as sources with high RM values are missed near the centre of the clusters due to depolarisation. Higher frequency data is required to more accurately constrain η using RM scatter only.

4. Jointly modelling both the depolarisation and rotation measure of sources in a forward modelling approach, we find that the observations best agree with the following magnetic field parameters: $B_0 = 5.0\,\mu$G, $\Lambda_{\rm max} = 300 - 1536$ kpc, $\eta = 0.5$ for a fixed Kolmogorov power spectrum with $n = 3.67$. Models with $n < 3$ are strongly rejected by the RM data.

5. We could not reject the null hypothesis that cluster members sources show similar scatter in $\sigma_{\rm RM}$ as background sources, consistent with the result that background sources and cluster members also show similar depolarisation in the same sample of clusters (Osinga et al., 2022).

6. The radial $\sigma_{\rm RM}$ profile of cool-core and non-cool-core clusters follows the expected trend from the thermal gas density profiles, with CC clusters showing a hint of larger $\sigma_{\rm RM}$ in the core, which significantly drops below the observed $\sigma_{\rm RM}$ of NCC clusters outside of the core, as the thermal gas density also drops rapidly outside of the core.

In this work, we implicitly assumed that all clusters have the same magnetic field parameters, while in reality, this might be a function of dynamical state, mass, or redshift. The universality of cluster magnetic fields has not been thoroughly tested (e.g. Govoni et al., 2017). Future observations with more sensitive telescopes such as MeerKAT and the SKA could test this assumption by detecting enough polarised sightlines through single clusters such that stacking is not required.

ACKNOWLEDGEMENTS

EO and RJvW acknowledge support from the VIDI research programme with project number 639.042.729, which is financed by the Netherlands Organisation for Scientific Research (NWO). EO thanks both Wout Goesaert and Joppe Swart for the careful looks at his code. This paper has made use of observational material taken with an NRAO instrument. The National Radio Astronomy Observatory is a facility of the National Science Foundation operated under cooperative agreement by Associated Universities, Inc. The Pan-STARRS1 Surveys (PS1) and the PS1 public science archive have been made possible through contributions by the Institute for Astronomy, the University of Hawaii, the Pan-STARRS Project Office, the Max-Planck Society and its participating institutes, the Max Planck Institute for Astronomy, Heidelberg and the Max Planck Institute for Extraterrestrial Physics, Garching, The Johns Hopkins University, Durham University, the University of Edinburgh, the Queen's University Belfast, the Harvard-Smithsonian Center for Astrophysics, the Las Cumbres Observatory Global Telescope Network Incorporated, the National Central University of Taiwan, the Space Telescope Science Institute, the National Aeronautics and Space Administration under Grant No. NNX08AR22G issued through the Planetary Science Division of the NASA Science Mission Directorate, the National Science Foundation Grant No. AST-1238877, the University of Maryland, Eotvos Lorand University (ELTE), the Los Alamos National Laboratory, and the Gordon and Betty Moore Foundation. The Legacy Surveys consist of three individual and complementary projects: the Dark Energy Camera Legacy Survey (DECaLS; Proposal ID 2014B-0404; PIs: David Schlegel and Arjun Dey), the Beijing-Arizona Sky Survey (BASS; NOAO Prop. ID 2015A-0801; PIs: Zhou Xu and Xiaohui Fan), and the Mayall z-band Legacy Survey (MzLS; Prop. ID 2016A-0453; PI: Arjun Dey). DECaLS, BASS and MzLS together include data obtained, respectively, at the Blanco telescope, Cerro Tololo Inter-American Observatory, NSF's NOIRLab; the Bok telescope, Steward Observatory, University of Arizona; and the Mayall telescope, Kitt Peak National Observatory, NOIRLab. The Legacy Surveys project is honoured to be permitted to conduct astronomical research on Iolkam Du'ag (Kitt Peak), a mountain with particular significance to the Tohono O'odham Nation. SDSS-IV is managed by the Astrophysical Research Consortium for the Participating Institutions of the SDSS Collaboration including the Brazilian Participation Group, the Carnegie Institution for Science, Carnegie Mellon University, Center for Astrophysics | Harvard & Smithsonian, the Chilean Participation Group, the French Participation Group, Instituto de Astrofísica de Canarias, The Johns Hopkins University, Kavli Institute for the Physics and Mathematics of the Universe (IPMU) / University of Tokyo, the Korean Participation Group, Lawrence Berkeley National Laboratory, Leibniz Institut für Astrophysik Potsdam (AIP), Max-Planck-Institut für Astronomie (MPIA Heidelberg), Max-Planck-Institut für Astrophysik (MPA Garching), Max-Planck-Institut für Extraterrestrische Physik (MPE), National Astronomical Observatories of China, New Mexico State University, New York University, University of Notre Dame, Observatário Nacional / MCTI, The Ohio State University, Pennsylvania State University, Shanghai Astronomical Observatory, United Kingdom Participation Group, Universidad Nacional Autónoma de México, University of Arizona, University of

Colorado Boulder, University of Oxford, University of Portsmouth, University of Utah, University of Virginia, University of Washington, University of Wisconsin, Vanderbilt University, and Yale University This research has made use of the NASA/IPAC Extragalactic Database (NED), which is operated by the Jet Propulsion Laboratory, California Institute of Technology, under contract with the National Aeronautics and Space Administration. This research has made use of NASA's Astrophysics Data System (ADS).

Appendix I: Additional plots

For completeness, we plot in Figures 6.17 and 6.18 the cluster-induced rotation measure on a linear scale as a function of projected radius and column density, respectively. The electron density profiles of the clusters in our sample, as determined in Andrade-Santos et al. (2017), are shown in Figure 6.19. The structure function as defined in Equation 6.14 is shown in Figure 6.20. Finally, the q values of the full forward model for $\eta = 0.1$ are shown in 6.21, with the best-fit profiles shown in Fig 6.22. For $\eta = 0.1$, there is a clear mismatch between the depolarisation and RM scatter profiles. The depolarisation favours low values of B_0 with high values of $\Lambda_{\rm max}$, while the RM scatter favours high values of B_0 with small values of $\Lambda_{\rm max}$. A model with $\eta = 0.5$ thus more naturally predicts the behaviour of both the RM scatter and depolarisation consistently.

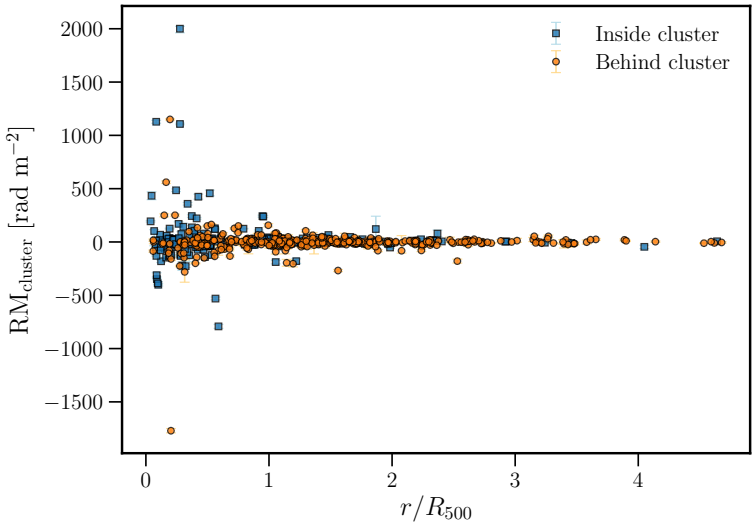

Figure 6.17: Cluster induced rotation measure as a function of normalised distance to the nearest cluster centre. The y-axis is shown on a linear scale, while a better view of sources with low RM is given by Figure 6.2.

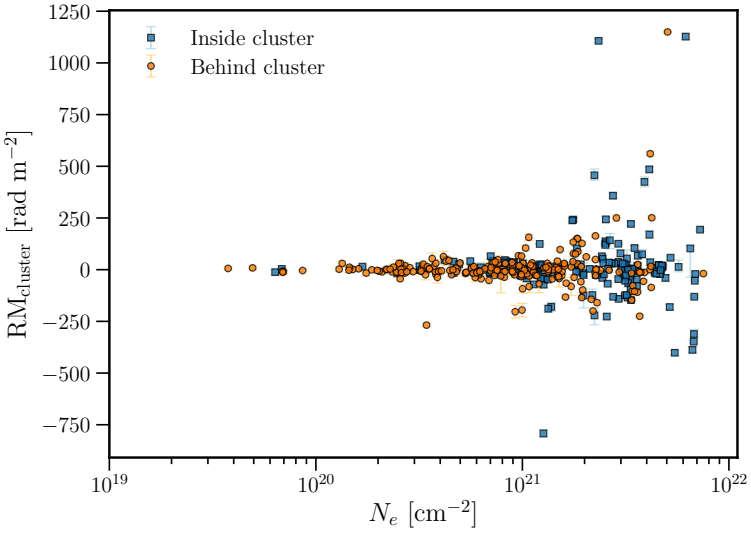

Figure 6.18: Cluster induced rotation measure as a function of electron column density. The y-axis is shown on a linear scale, while a better view of sources with low RM is given by Figure 6.4.

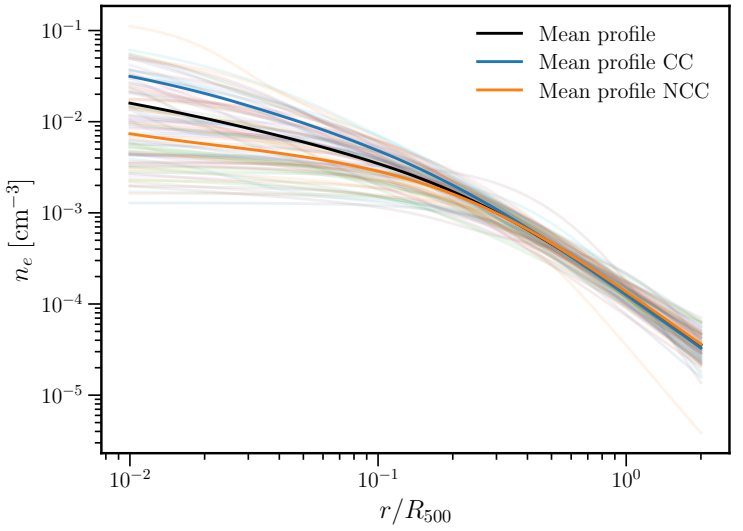

Figure 6.19: Average electron density profile as a function of normalised 3D radius for all clusters that have Chandra X-ray observations. The mean profile is shown in the black line.

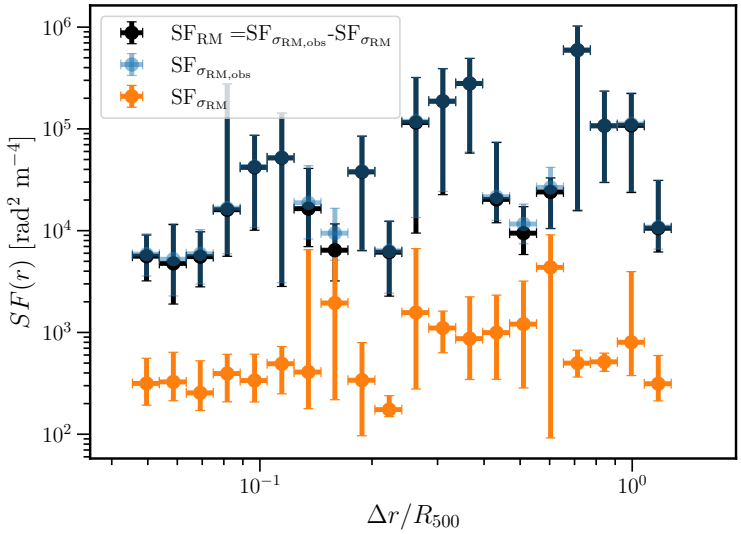

Figure 6.20: Corrected RM structure function as defined in Eq 6.14 as a function of normalised pair separation in 20 logarithmically spaced bins. The total RM structure function and the relatively small offset correction are shown in blue and orange respectively.

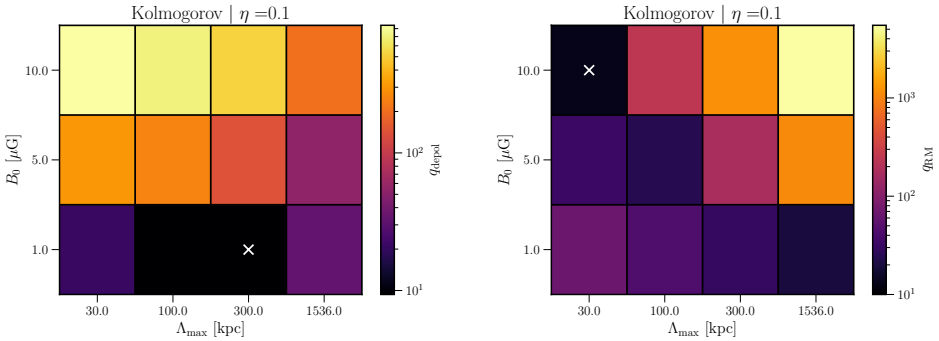

(a) (b)

Figure 6.21: Values of q_{depol} (a) and q_{RM} (b) as defined in Equation 6.15 for combinations of B_0 and Λ_{RM}. Models are simulated with a Kolmogorov power spectrum and $\eta = 0.1$. The best-fit model is marked by a cross.

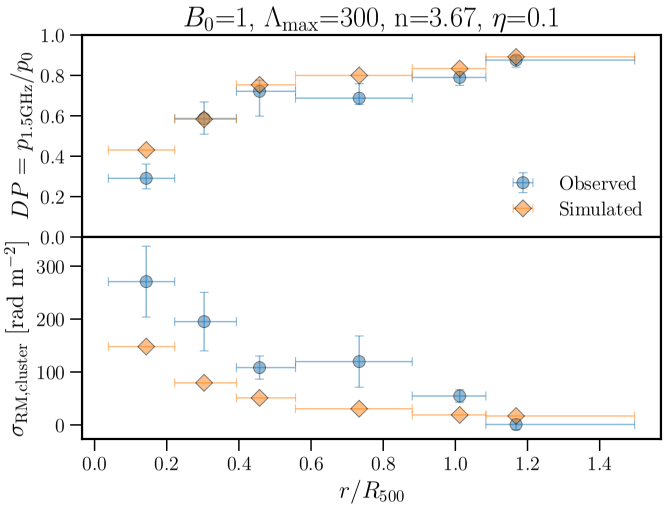

(a) Model that minimizes q_{depol}.

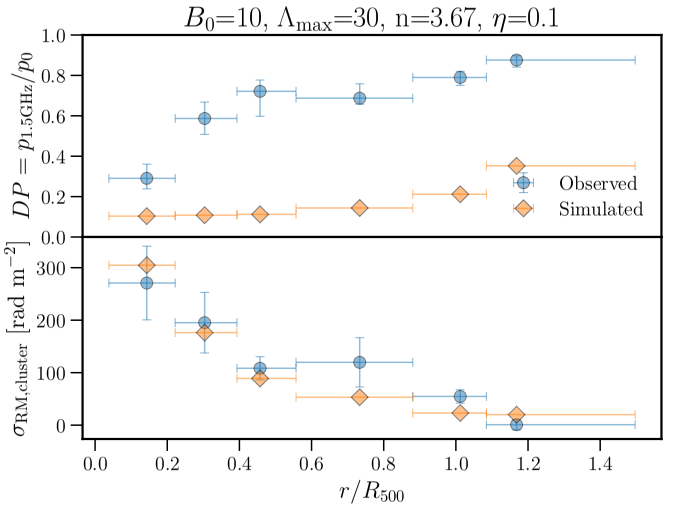

(b) Model that minimizes q_{RM}.

Figure 6.22: Comparison between observed and forward-simulated depolarisation and RM scatter for the model with $\eta = 0.1$ that minimizes the q statistics as defined in Equation 6.15.

Appendix II: Radial RM scatter

Here we investigate how to quantify the radial RM scatter in more detail than in Section 6.4.2, where the sample standard deviation was used. Figures 6.6 and Fig. 6.10 showed the scatter calculated from the standard deviation and interquartile range respectively. For a Gaussian distribution, it should hold that the standard deviation is equal to IQR/1.35, but this is clearly not the case. This is expected, however, as the distribution of RMs is only expected to be Gaussian at a single projected radius. In a radial bin of finite size, we are thus observing the sum of Gaussian distributions with different standard deviations, leading to a non-Gaussian distribution. This poses the question of how to best quantify the scatter. In Figure 6.24, we show the full RM distribution in the radial bins of Figures 6.6 and Fig. 6.10. Gaussian distributions with scatter calculated from the IQR and sample standard deviation are shown in the coloured lines. The IQR always shows a better fit to the central peak of the distribution, but underestimates the tails of the distribution. Vice versa, the standard deviation captures the tails of the distribution better but underestimates the central peaks. To compare the effect of the different estimates on the result of Section 6.4.2, we also fit the scatter calculated from the IQR to the theoretical RM scatter profile. The results are shown in Figures 6.23 and 6.25. Because the IQR is less sensitive to the excess in sources with high RM observed near the centre of clusters, the profile is flatter than the sample standard deviation radial profile, and we can thus not constrain η in this way. The resulting central magnetic field dispersion is about a factor 3 lower when calculated by means of IQR than through sample standard deviation.

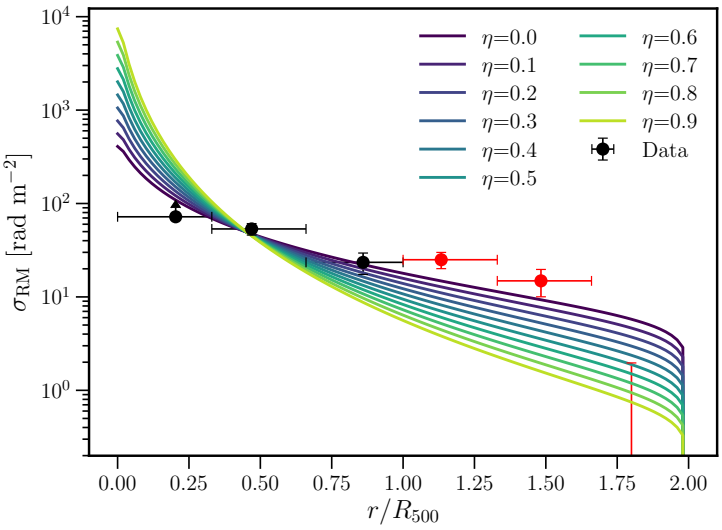

Figure 6.23: RM scatter calculated from the IQR and corrected for a baseline value of $\sigma_{\mathrm{RM}} = 15$ as a function of projected distance. The first point is plotted as a lower limit, and points outside R_{500} (shown in red) are ignored in the fit. The coloured lines show best-fit profiles computed for various values of η assuming Equation 6.10. The coloured lines show best-fit profiles computed for various values of η.

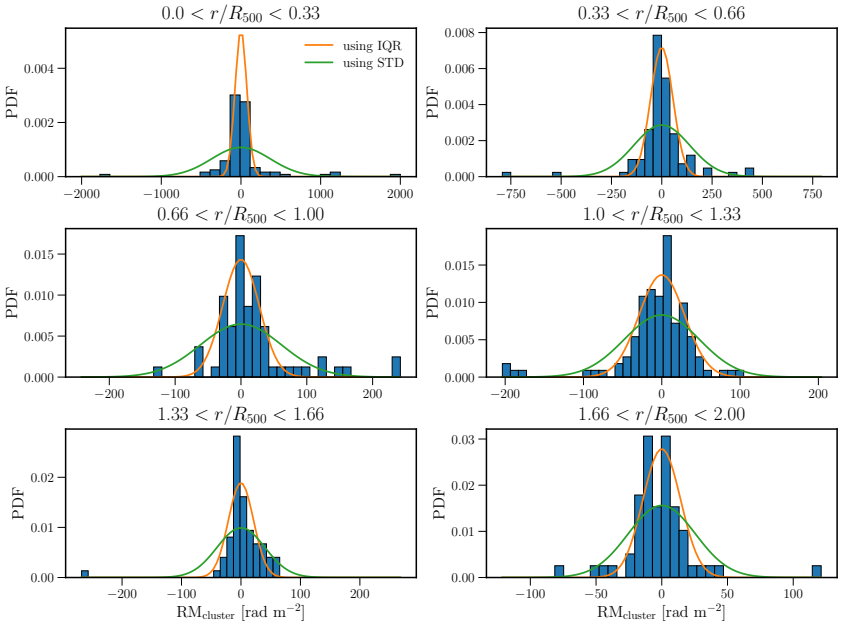

Figure 6.24: Distribution of RMs in different radial bins. The scatter is quantified in two ways, using the standard deviation and the interquartile range divided by 1.35.

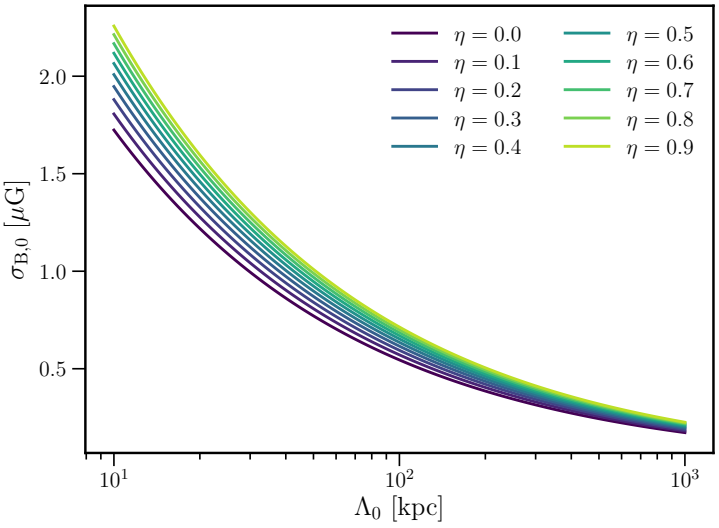

Figure 6.25: Central magnetic field dispersion as a function of the characteristic length scale Λ_0 and the magnetic field to thermal electron density scaling parameter η.

Appendix III: Updated polarised source catalogue

Table F.1: First 30 rows of the catalogue of 819 polarised radio sources that were detected in this work. The full table will become available in electronic form at the Centre de Données astronomiques de Strasbourg (CDS).

RA [deg]	DEC [deg]	Maj [″]	Min [″]	PA [deg]	p_0	χ_0 [rad]	RM [rad m^{-2}]	$\sigma_{\rm RM}$ [rad^2 m^{-4}]	I_0 [mJy]	α	$\tilde{\chi}^2_{\rm QU}$	$z_{\rm best}$	$z_{\rm best}$ source	$\theta_{\rm P}$ [arcmin]	r/R_{500}	Cluster	RA$_{\rm opt}$ [deg]	DEC$_{\rm opt}$ [deg]	MC	Flagged	Note	RM$_{\rm cluster}$ [rad m^{-2}]
19.55453 ± 0.00009	−27.16767 ± 0.00010	10.4 ± 1.1	6.11 ± 0.35	136 ± 7	$0.127^{+0.046}_{-0.030}$	$2.975^{+3.154}_{-3.154}$	20^{+6}_{-5}	8^{+5}_{-3}	$5.0^{+0.2}_{-0.2}$	$-0.45^{+0.12}_{-0.13}$	61	0.948 ± 0.077	2	11.60	2.9	G212.97-84.04	19.5606	-27.1622	False	False		10^{+11}_{11}
15.794198 ± 0.000035	−21.996243 ± 0.000030	7.03 ± 0.31	6.29 ± 0.24	117 ± 16	$0.079^{+0.029}_{-0.021}$	$0.995^{+0.498}_{-0.498}$	30^{+7}_{-7}	13^{+3}_{-3}	$12.7^{+0.2}_{-0.2}$	$-0.88^{+0.04}_{-0.04}$	52	-	-	9.49	0.6	G149.55-84.16	-	-	False	False	No counterpart.	27^{+9}_{8}
41.4094860 ± 0.0000022	−20.6108492 ± 0.0000024	9.548 ± 0.021	8.841 ± 0.018	59.7 ± 1.2	$0.104^{+0.001}_{-0.001}$	$0.465^{+0.008}_{-0.008}$	14^{+0}_{-0}	2^{+0}_{-0}	149.1^{+18}_{-18}	$-0.68^{+0.03}_{-0.03}$	434	-	-	12.41	3.5	G205.07-62.94	-	-	False	True	No counterpart.	13^{+5}_{5}
41.411690 ± 0.000009	−20.580840 ± 0.000007	9.18 ± 0.08	8.14 ± 0.06	101.3 ± 2.9	$0.119^{+0.003}_{-0.003}$	$1.643^{+3.117}_{-3.117}$	17^{+1}_{-1}	2^{+1}_{-1}	$28.6^{+0.4}_{-0.4}$	$-0.84^{+0.04}_{-0.04}$	144	-	-	11.75	3.3	G205.07-62.94	-	-	False	True	No counterpart.	18^{+6}_{6}
40.48671 ± 0.00010	−28.63936 ± 0.00021	30.8 ± 1.9	10.4 ± 0.4	113.9 ± 3.3	$0.281^{+0.024}_{-0.024}$	$0.368^{+0.071}_{-0.071}$	8^{+1}_{-1}	7^{+1}_{-1}	$16.1^{+0.5}_{-0.5}$	$-1.61^{+0.08}_{-0.08}$	89	0.238 ± 0.000	1	6.43	1.6	G222.97-65.69	40.4839	-28.6379	True	True	Radio Relic.	5^{+5}_{5}
40.47708 ± 0.00020	−28.63432 ± 0.00015	20.7 ± 2.0	10.0 ± 0.6	124 ± 6	$0.296^{+0.063}_{-0.054}$	$0.187^{+0.153}_{-0.153}$	7^{+3}_{-3}	10^{+2}_{-2}	$9.7^{+0.4}_{-0.4}$	$-2.37^{+0.13}_{-0.13}$	80	0.238 ± 0.000	1	5.95	1.5	G222.97-65.69	40.4839	-28.6379	True	True	Radio Relic.	3^{+6}_{6}
40.48939 ± 0.00025	−28.65367 ± 0.00018	20.5 ± 2.3	14.8 ± 1.4	114 ± 16	$0.140^{+0.014}_{-0.014}$	$1.909^{+3.123}_{-3.123}$	6^{+3}_{-3}	2^{+2}_{-1}	$9.6^{+0.4}_{-0.4}$	$-1.09^{+0.10}_{-0.10}$	88	0.238 ± 0.000	1	6.56	1.6	G222.97-65.69	40.4839	-28.6379	True	True	Radio Relic.	2^{+6}_{6}
40.4898 ± 0.0005	−28.64934 ± 0.00008	46 ± 4	10.2 ± 0.5	96 ± 4	$0.292^{+0.033}_{-0.031}$	$1.754^{+2.969}_{-2.969}$	9^{+2}_{-2}	6^{+1}_{-1}	$13.9^{+0.6}_{-0.6}$	$-1.89^{+0.12}_{-0.13}$	133	0.238 ± 0.000	1	6.57	1.6	G222.97-65.69	40.4839	-28.6379	True	True	Radio Relic.	7^{+5}_{5}
40.47123 ± 0.00030	−28.63765 ± 0.00029	29.7 ± 3.2	17.2 ± 1.5	134 ± 11	$0.190^{+0.042}_{-0.035}$	$2.022^{+2.799}_{-2.799}$	7^{+3}_{-3}	9^{+2}_{-2}	$20.3^{+0.7}_{-0.7}$	$-2.48^{+0.10}_{-0.10}$	88	0.238 ± 0.000	1	5.62	1.4	G222.97-65.69	40.4839	-28.6379	True	True	Radio Relic.	4^{+7}_{7}
40.33575 ± 0.00011	−28.40285 ± 0.00006	10.4 ± 1.0	7.1 ± 0.4	104 ± 9	-	-	-	-	-	-	-	1.135 ± 0.185	2	14.75	3.5	G222.97-65.69	-	-	True	True	No counterpart.	-
40.33588 ± 0.00004	−28.41099 ± 0.00004	10.4 ± 0.4	7.16 ± 0.18	138 ± 4	$0.034^{+0.005}_{-0.005}$	$1.832^{+2.927}_{-2.927}$	17^{+3}_{-3}	8^{+2}_{-1}	$52.3^{+0.7}_{-0.7}$	$-0.96^{+0.03}_{-0.03}$	90	1.135 ± 0.185	2	14.27	3.4	G222.97-65.69	40.3352	-28.4072	True	False		19^{+6}_{9}
10.94092 ± 0.00004	−20.49858 ± 0.00004	9.5 ± 0.4	7.56 ± 0.25	143 ± 8	$0.040^{+0.009}_{-0.006}$	$0.600^{+0.152}_{-0.152}$	-10^{+3}_{-3}	7^{+3}_{-2}	$17.1^{+0.3}_{-0.3}$	$-0.71^{+0.04}_{-0.04}$	72	0.414 ± 0.068	2	8.55	2.3	G106.73-83.22	10.9412	-20.4988	False	False		-21^{+9}_{9}
10.79686 ± 0.00014	−20.53360 ± 0.00005	22.8 ± 1.2	11.9 ± 0.4	84 ± 4	$0.215^{+0.025}_{-0.024}$	$2.473^{+3.143}_{-3.143}$	-6^{+2}_{-2}	7^{+1}_{-1}	$15.0^{+0.5}_{-0.5}$	$-1.85^{+0.10}_{-0.10}$	89	0.281 ± 0.013	2	5.25	1.4	G106.73-83.22	10.7947	-20.5365	False	False		-16^{+8}_{8}
10.75281 ± 0.00012	−20.58744 ± 0.00006	18.1 ± 1.2	6.67 ± 0.17	155.7 ± 2.4	$0.079^{+0.009}_{-0.008}$	$2.442^{+3.143}_{-3.143}$	-12^{+2}_{-2}	6^{+2}_{-1}	$18.3^{+0.4}_{-0.4}$	$-1.12^{+0.05}_{-0.05}$	75	0.729 ± 0.067	2	5.31	1.4	G106.73-83.22	10.7440	-20.5799	True	False		-24^{+8}_{8}
10.74349 ± 0.00005	−20.62051 ± 0.00012	14.2 ± 1.1	6.54 ± 0.22	159.5 ± 3.4	$0.001^{+0.000}_{-0.000}$	$0.238^{+0.182}_{-0.182}$	18^{+4}_{-4}	8^{+3}_{-2}	$478.9^{+5.4}_{-5.3}$	$-0.83^{+0.03}_{-0.02}$	184	0.281 ± 0.272	2	5.72	1.5	G106.73-83.22	10.7432	-20.6204	True	True		24^{+9}_{10}
10.743987 ± 0.000028	−20.57991 ± 0.00004	8.81 ± 0.35	7.17 ± 0.22	160 ± 7	$0.004^{+0.001}_{-0.001}$	$2.045^{+3.144}_{-3.144}$	-157^{+4}_{-4}	7^{+4}_{-3}	$134.3^{+1.5}_{-1.5}$	$-0.53^{+0.03}_{-0.02}$	57	0.729 ± 0.067	2	5.91	1.6	G106.73-83.22	10.7440	-20.5799	True	False		-268^{+9}_{9}
10.73185 ± 0.00011	−20.57074 ± 0.00017	14.4 ± 1.4	11.5 ± 1.0	172 ± 19	$0.090^{+0.016}_{-0.012}$	$1.111^{+0.206}_{-0.206}$	-3^{+4}_{-3}	6^{+3}_{-2}	$9.5^{+0.3}_{-0.3}$	$-0.60^{+0.08}_{-0.08}$	73	0.729 ± 0.067	2	6.73	1.8	G106.73-83.22	10.7440	-20.5799	True	False		-11^{+9}_{9}
10.8157	-20.5492	8.2	8.2	0	$0.192^{+0.047}_{-0.036}$	$2.975^{+3.151}_{-3.151}$	-19^{+4}_{-4}	6^{+3}_{-2}	$3.2^{+0.3}_{-0.3}$	$-2.24^{+0.25}_{-0.24}$	71	0.603 ± 0.041	2	3.93	1.0	G106.73-83.22	10.8167	-20.5483	False	False		-37^{+10}_{10}
46.89273 ± 0.00006	−28.725980 ± 0.000029	7.1 ± 0.5	5.03 ± 0.22	106 ± 7	$0.439^{+0.335}_{-0.271}$	$0.060^{+0.864}_{-0.864}$	85^{+76}_{-75}	41^{+5}_{-8}	$11.8^{+0.2}_{-0.2}$	$-0.57^{+0.04}_{-0.04}$	125	0.270 ± 0.020	2	7.51	1.9	G223.91-60.09	46.8925	-28.7259	False	False		121^{+120}_{119}
46.83815 ± 0.00017	−28.68291 ± 0.00004	13.7 ± 1.5	6.18 ± 0.30	95 ± 5	$0.033^{+0.018}_{-0.010}$	$2.496^{+3.154}_{-3.154}$	41^{+8}_{-7}	12^{+6}_{-3}	$20.1^{+0.3}_{-0.3}$	$-0.85^{+0.03}_{-0.03}$	78	0.383 ± 0.035	2	3.98	1.1	G223.91-60.09	46.8365	-28.6812	True	False		53^{+15}_{15}
46.83576 ± 0.00015	−28.67959 ± 0.00021	17.2 ± 2.2	6.00 ± 0.30	145 ± 5	$0.072^{+0.048}_{-0.023}$	$2.646^{+3.160}_{-3.160}$	42^{+20}_{-15}	24^{+7}_{-4}	$25.1^{+0.3}_{-0.4}$	$-0.76^{+0.03}_{-0.03}$	72	0.383 ± 0.035	2	3.83	1.1	G223.91-60.09	46.8365	-28.6812	True	False		55^{+32}_{23}
46.83814 ± 0.00005	−28.68534 ± 0.00005	7.2 ± 0.5	5.38 ± 0.26	138 ± 9	$0.046^{+0.557}_{-0.023}$	$2.559^{+3.139}_{-3.139}$	78^{+26}_{-65}	19^{+3187}_{-6}	$11.9^{+0.2}_{-0.2}$	$-0.71^{+0.04}_{-0.04}$	60	0.383 ± 0.035	2	4.00	1.1	G223.91-60.09	46.8365	-28.6812	True	False		111^{+41}_{103}
357.900782 ± 0.000032	−25.938221 ± 0.000018	7.68 ± 0.28	5.76 ± 0.15	102 ± 5	$0.038^{+0.008}_{-0.006}$	$0.442^{+0.182}_{-0.182}$	-26^{+4}_{-4}	7^{+3}_{-2}	$16.5^{+0.2}_{-0.2}$	$-0.55^{+0.04}_{-0.04}$	63	0.187 ± 0.133	3	8.47	2.0	G034.03-76.59	357.9006	-25.9388	False	False		-52^{+9}_{9}
156.14934 ± 0.00006	−27.20391 ± 0.00004	7.9 ± 0.6	6.10 ± 0.31	112 ± 10	$0.040^{+0.019}_{-0.013}$	$2.451^{+3.040}_{-3.040}$	49^{+12}_{-9}	16^{+5}_{-4}	$13.3^{+0.2}_{-0.2}$	$-0.39^{+0.04}_{-0.04}$	111	0.258 ± 0.163	3	10.01	2.4	G266.84+25.07	156.1492	-27.2033	False	False		79^{+33}_{30}
156.02742 ± 0.00005	−27.331459 ± 0.000032	8.4 ± 0.4	7.05 ± 0.27	90 ± 10	$0.058^{+0.015}_{-0.012}$	$0.385^{+0.212}_{-0.212}$	-128^{+6}_{-6}	15^{+3}_{-2}	$10.8^{+0.2}_{-0.2}$	$-0.78^{+0.04}_{-0.04}$	95	-	-	4.83	1.1	G266.84+25.07	-	-	False	False	No counterpart.	-196^{+32}_{32}
155.935295 ± 0.000027	−27.34246 ± 0.00004	8.82 ± 0.34	7.21 ± 0.22	11 ± 7	$0.069^{+0.014}_{-0.012}$	$1.115^{+1.386}_{-1.386}$	-133^{+7}_{-7}	20^{+2}_{-2}	$17.3^{+0.3}_{-0.3}$	$-0.55^{+0.04}_{-0.03}$	139	-	-	5.06	1.2	G266.84+25.07	-	-	False	False	No counterpart.	-204^{+30}_{31}
155.723060 ± 0.000033	−27.180613 ± 0.000032	9.01 ± 0.29	8.66 ± 0.26	116 ± 33	$0.025^{+0.004}_{-0.003}$	$0.873^{+0.147}_{-0.147}$	-9^{+3}_{-2}	5^{+2}_{-2}	$43.3^{+0.6}_{-0.6}$	$-1.01^{+0.03}_{-0.04}$	138	-	-	14.38	3.4	G266.84+25.07	-	-	False	False	No counterpart.	-173^{+40}_{40}
172.93573 ± 0.00008	−19.87149 ± 0.00008	8.0 ± 0.7	7.7 ± 0.6	(1.4 ± 0.8)e+02	$0.309^{+0.528}_{-0.216}$	$0.080^{+0.825}_{-0.825}$	-132^{+1279}_{-733}	$76^{+3737525578}_{-35}$	$2.6^{+0.2}_{-0.2}$	$-0.73^{+0.14}_{-0.13}$	83	0.291 ± 0.025	3	5.23	1.3	G278.60+39.17	172.9325	-19.8793	True	True		-208^{+2186}_{1252}
172.932507 ± 0.000035	−19.87992 ± 0.00007	13.5 ± 0.6	8.47 ± 0.23	20 ± 4	$0.044^{+0.005}_{-0.005}$	$2.789^{+3.142}_{-3.142}$	-0^{+2}_{-3}	4^{+2}_{-2}	$10.0^{+0.3}_{-0.3}$	$-0.95^{+0.06}_{-0.06}$	152	0.291 ± 0.025	3	5.03	1.2	G278.60+39.17	172.9325	-19.8793	True	True		18^{+19}_{19}
172.93171 ± 0.00005	−19.88390 ± 0.00005	9.1 ± 0.5	8.00 ± 0.35	139 ± 16	$0.078^{+0.018}_{-0.016}$	$2.825^{+3.149}_{-3.149}$	-115^{+6}_{-7}	14^{+3}_{-2}	$4.8^{+0.2}_{-0.2}$	$-0.69^{+0.08}_{-0.08}$	141	0.291 ± 0.025	3	4.93	1.2	G278.60+39.17	172.9325	-19.8793	True	False		-180^{+21}_{22}

Notes. The columns are identical to Osinga et al. (2022), with MC denoting whether a source has multiple components. The only newly added column is RM$_{\rm cluster}$, which is defined in Equation 6.3. If uncertainties are not available, they are not given.